Title

Hydrogen production using curtailed electricity of firm photovoltaic plants: Conception, modeling, and optimization

Authors
Yang, Guoming
Yang, Dazhi
Perez, Marc J
et al.

Publication Date
2024-05-01

DOI
10.1016/j.enconman.2024.118356

Hydrogen production using curtailed electricity of firm photovoltaic plants: Conception, modeling, and optimization

Guoming Yang[a], Dazhi Yang[a,*], Marc J. Perez[b], Richard Perez[c], Jan Kleissl[d], Jan Remund[e], Marco Pierro[f], Yuan Cheng[a], Yi Wang[g], Xiang'ao Xia[h,i], Jianing Xu[a], Chao Lyu[a], Bai Liu[a], Hao Zhang[a,**]

[a] *School of Electrical Engineering and Automation, Harbin Institute of Technology, Harbin, Heilongjiang, China*
[b] *Clean Power Research, Napa, CA 94559 USA*
[c] *Atmospheric Sciences Research Center, University at Albany, SUNY, Albany, NY 12222 USA*
[d] *Department of Mechanical and Aerospace Engineering, University of California, San Diego, CA, USA*
[e] *Meteotest, Fabrikstrasse 14, CH-3012 Bern, Switzerland*
[f] *EURAC Research, Viale Druso, 1, 39100, Bolzano, Italy*
[g] *Department of Electrical and Electronic Engineering, The University of Hong Kong, Hong Kong Special Administrative Region of China*
[h] *Key Laboratory of Middle Atmosphere and Global Environment Observation, Institute of Atmospheric Physics, Chinese Academy of Sciences, Beijing 10029, China*
[i] *University of Chinese Academy of Sciences, Beijing 100049, China*

Abstract

A firm photovoltaic (PV) plant differs from a conventional unconstrained PV plant in terms of its ability to satisfy load demand on a 24/365 basis. Amongst various firm power enablers, overbuilding & proactive curtailment is the most counter-intuitive yet indispensable one. Although the cost-effectiveness of firm PV plants has been studied numerous times, few studies have evaluated the utilization of curtailed energy. To that end, this work advocates using the curtailed energy for hydrogen production, which is not impacted by the intermittency and variability of the curtailed power. A new mathematical optimization model that minimizes the firm kWh premium of the PV–battery–hydrogen hybrid system is put forth. Instead of using just generic modeling for the energy components (i.e., PV, battery, and electrolyzer), refined modeling, which could introduce bilinearity and nonlinearity, is herein considered. To address such optimization difficulty, a new algorithm, which hybridizes the particle swarm optimization and the branch-and-bound method, is proposed. The analysis reveals that the additional inclusion of a hydrogen production system within a firm PV plant is techno-economically attractive, and can lower the curtailment rate by 36%, and the overall firm kWh premium by almost 7%. What this implies is that, under the current market economics, the hydrogen production system becomes entirely free when used with firm PV plants.

Highlights

- A firm photovoltaic–battery–hydrogen hybrid system is proposed.
- The hybrid system is able to meet demand 24/365 with 100% certainty.
- A hybrid algorithm is proposed for the nonlinear optimization problem.
- Power curtailment is necessary to achieve the lowest system cost.

Keywords: Firm generation, Firm photovoltaic plant, Curtailment, Hydrogen production, Refined model

*The two authors have the same contribution to this study.
**Corresponding author.
Email addresses: yangdazhi.nus@gmail.com (Dazhi Yang), zh_hit@hit.edu.cn (Hao Zhang)

Nomenclature

Indices

b	Quantities related to battery storage
comp	Quantities related to a compressor
d	Index of the dimensions of the PSO algorithm
elec	Quantities related to an electrolyzer
$i \in \mathcal{I}$	Charging measurements of battery storage
$l \in \mathcal{L}$	Line segment in the piecewise linear fitting
m	Index of the particles of the PSO algorithm
$o \in \mathcal{O}$	Discharging measurements of battery storage
s	Quantities related to the solar power
$t \in \mathcal{T}$	Time stamps, which index the 8760 hours in a year
tank	Quantities related to hydrogen tank
$y \in \mathcal{Y}$	Energy components configured in the hybrid system

Constants

a_l	Slope of the l^{th} line segment, kg/kWh
A	Cross-sectional area of an electrolyte cell, m^2
b_l	Intercept of the l^{th} line segment, kg/h
B_n	Beam normal irradiance, W/m^2
c	Unit investment cost, \$/kW or \$/kWh or $\$/\text{m}^3$
c_1	Individual learning factor, dimensionless
c_2	Social learning factor, dimensionless
$\overline{d}$	Number of variables solved by the PSO algorithm, dimensionless
D_h	Diffuse horizontal irradiance, W/m^2
D_H	Hydrogen diffusivity coefficient under the operating temperature (T_0), m^2/s
e_A	Anodic current collector thickness, m
e_C	Cathodic current collector thickness, m
e_M	Average membrane thickness, m
F	Faraday constant, C/mol
f_{gbest}	Optimal fitness value of all particles before j^{th} iteration, \$
f_m^j	Fitness value of each particle, \$
$f_{m,\text{pbest}}$	Optimal fitness value of m^{th} particle before j^{th} iteration, \$
f_{PV}	PV derating factor, dimensionless
G_c	Global tilted irradiance, W/m^2
G_c'	Effective irradiance, W/m^2
G_h	Global horizontal irradiance, W/m^2
i	Current density of an electrolyte cell, A/m^2
$\widetilde{i}$	Rated value of i, A/m^2
$i_{0\text{A}}$	Anodic exchange current density, A/m^2
I	Current flowing through the electrolyte cell, A
$\widetilde{I}$	Rated value of I, A
I_{loss}	Loss current of an electrolyte cell, A
H_h	Hydrogen high heating value, kWh/kg
$\overline{j}$	Maximum iteration number, dimensionless
k	Average electrolyte conductivity, S/m
l	Equivalent annual operation and maintenance factor, dimensionless
$\overline{m}$	Number of particles, dimensionless
$\overline{N}_b$	Maximum value allowed for N_b, dimensionless
p	Parameter of the empirical Sandia Array Performance Model, dimensionless
P_{ac}	AC power output of the inverter, W
$\widetilde{P}_{\text{ac}}$	Rated output power of the inverter, W
$\widehat{P}_{\text{ch},i}$	Measurement value of $P_{\text{ch},t}$, kWh
P_{dc}	DC power output of PV modules, W
$\widehat{P}_{\text{dis},o}$	Measurement value of $P_{\text{dis},t}$, kWh
$\overline{P}_{\text{elec}}$	Upper limit value of the rated power of the electrolyzer, kW
$P^0_{\text{elec},l}$	Left endpoint of the l^{th} line segment, kW
$P^0_{\text{elec},l+1}$	Right endpoint of the l^{th} line segment, kW
p_{gbest}	Position of the particle with the population optimum before j^{th} iteration, kW or dimensionless

PGF	Panel generation factor, dimensionless
$\widehat{P}_{\mathrm{in},i}$	Measurement value of $P_{\mathrm{in},t}$, kWh
$P_{\mathrm{load},t}$	Load demand at time t, kW
$p_{m,\mathrm{pbest}}$	Position of the m^{th} particle with the individual optimum before j^{th} iteration, kW or dimensionless
$\widehat{P}_{\mathrm{out},o}$	Measurement value of $P_{\mathrm{out},t}$, kWh
P_{pv}	AC power output of the PV system, W
$P_{\mathrm{pv},t}$	Output power of the unconstrained PV plant at time t, kW
$\widetilde{P}_s$	Rated power of the PV plant, W
q	Parameter of the empirical Sandia Array Performance Model, dimensionless
r_1/r_2	Random numbers generated following a uniform distribution between 0 and 1, dimensionless
R	Ideal gas constant, J/(mol·K)
R_0	Ohmic resistance of an electrolyte cell, Ω
R_d	Diffuse transposition factor, dimensionless
R_r	Transposition factor due to ground reflection, dimensionless
S	Tilt angle of the PV array, °
$S_{b,\mathrm{ref}}$	Rated capacity of the testing battery from which the charging and discharging measurements were acquired, kWh
$\widehat{\mathrm{SoC}}_{\mathrm{ch},i}$	Measurement value of SoC_t when the battery is charging, dimensionless
$\widehat{\mathrm{SoC}}_{\mathrm{dis},o}$	Measurement value of SoC_t when the battery is discharging, dimensionless
S_H	Hydrogen solubility coefficient under the operating temperature (T_0), mol/(pa·m^3)
T	Lifetime of the corresponding component, year
T_0	Operating temperature of the electrolyzer, K
T_{amb}	Ambient temperature, °C
T_{cell}	Cell temperature, °C
T_{mod}	Module temperature, °C
$T_{\mathrm{mod}}^{\mathrm{NOCT}}$	Nominal operating cell temperature of PV modules, °C
U_A	Anodic over-potential, V
U_C	Cathodic over-potential, V
U_{cell}	Operating cell voltage, V
$\widetilde{U}_{\mathrm{cell}}$	Rated value of U_{cell}, V
U_{rev}	Reversible cell voltage, V
V	Wind speed at a height of 10 meters, m/s
$\overline{v}_d$	Maximum particle velocity, kW or dimensionless
$\underline{v}_d$	Minimum particle velocity, kW or dimensionless
$v_{m,d}^j$	Velocity of each particle, kW or dimensionless
$\overline{w}$	Maximum inertia weight, dimensionless
$\underline{w}$	Minimum inertia weight, dimensionless
$x_{m,d}^j$	Position of each particle, kW or dimensionless
$\overline{X}_s$	Upper limit of the PV oversizing ratio, dimensionless
z	Stoichiometric coefficient, dimensionless
Z	Solar zenith angle, °
ΔP	Pressure difference across the electrolyzer membrane, pa
Δt	Time interval, which is equal to 1 h, h
ΔT	Parameter of the empirical Sandia Array Performance Model, °C
Variables	
$B_{\mathrm{ch},t}$	Binary variables indicating the battery charging state, dimensionless
$B_{\mathrm{dis},t}$	Binary variables indicating the battery discharging state, dimensionless
$B_{\mathrm{elec},l,t}$	Binary variable representing the status of the l^{th} line segment, dimensionless
$D_{\mathrm{elec,t}}$	Hydrogen production rate of the electrolyzer, kg/h
$D_{H,t}$	Volume of hydrogen for sale at time t, kg
$E_{b,t}$	Electrical energy stored in the battery storage, kWh
N_b	Number of batteries configured in the hybrid system, which is relaxed to a positive real number, dimensionless
N_b^*	Optimal number of battery storage, which is acquired by the hybrid algorithm, dimensionless
$P_{\mathrm{ch},t}$	Charging power of battery storage, kW
$\widetilde{P}_{\mathrm{comp}}$	Rated power of the compressor, kW
$P_{\mathrm{comp}}^{\mathrm{ref}}$	Reference hourly energy consumption of the compressor when compressing 1 kg of hydrogen, kWh/kg
$P_{\mathrm{comp},t}$	Input power of the compressor, kW
$P_{\mathrm{cur},t}$	PV power curtailment, kW
$P_{\mathrm{dir},t}$	Par of the power output of the PV plant, which is used to directly fulfill the load demand, kW
$P_{\mathrm{dis},t}$	Discharging power of battery storage, kW
$\widetilde{P}_{\mathrm{elec}}$	Rated power of the electrolyzer, kW
P_{elec}^*	Optimal rated power of the electrolyzer, which is acquired by the hybrid algorithm, kW
$P_{\mathrm{elec},t}$	Input power of the electrolyzer, kW

$P_{\text{elec},l,t}$	Input power corresponding to the l^{th} line segment at time t, kW
$P_{\text{in},t}$	Power that enters battery storage at time t before the battery efficiency have been considered, kW
$P_{\text{out},t}$	Power that leaves battery storage at time t after the battery efficiency have been considered, kW
S_b	Rated capacity of battery storage, kWh
SoC_t	State of charge of battery storage, dimensionless
$\widetilde{S}_{\text{tank}}$	Rated capacity of the tank, m^3
$S_{\text{tank},t}$	Volume of hydrogen stored in the tank at time t, m^3
$x_{i,t}$	Weight associated with the i^{th} battery charging measurement point, dimensionless
$x_{o,t}$	Weight associated with the o^{th} battery discharging measurement point, dimensionless
X_s	Oversizing ratio of the PV plant, dimensionless
$\eta_{\text{ch},t}$	Time-varying battery charging efficiency, dimensionless
$\eta_{\text{dis},t}$	Time-varying battery discharging efficiency, dimensionless
Greek letters	
α	Solar azimuth angle, °
α_A	Charge transfer coefficient at the anodic side, dimensionless
γ_A	Anodic rugosity factor, dimensionless
γ_{mod}	Temperature coefficient of the PV module, %/°C
η_{cell}	Efficiency of an electrolyte cell , %
$\eta_{\text{ch}}^{\text{ref}}$	Charging efficiency of battery storage, %
$\eta_{\text{dis}}^{\text{ref}}$	Discharging efficiency of battery storage, %
η_{elec}	Time-varying hydrogen production efficiency of the electrolyzer, %
$\eta_{\text{elec}}^{\text{ref}}$	Reference hydrogen production efficiency of the electrolyzer, %
η_I	Current efficiency of an electrolyte cell ,%
η_U	Voltage efficiency of an electrolyte cell ,%
η_{inv}	Time-varying inverter efficiency, %
$\eta_{\text{inv}}^{\text{norm}}$	Nominal efficiency of the inverter, %
θ	Incidence angle, °
ϑ_0	Standard atmospheric pressure, bar
ϑ_{comp}	Normal working pressure of the compressor, bar
$\vartheta_{\text{comp}}^{\text{ref}}$	Standard working pressure of the compressor, bar
λ_H	Hydrogen sale price, \$/kg
ξ	Capital recovery factor, dimensionless
ρ	Foreground albedo, dimensionless
ρ_{ld}	Load ratio of the electrolyzer, dimensionless
σ_A	Conductivity of the anodic current collector, S/m
σ_b	Self-discharge rate, %
σ_C	Conductivity of the cathodic current collector, S/m
τ_0	Discount rate, %
τ_b	Relative transmittance adjusted for beam radiation, dimensionless
τ_d	Relative transmittance adjusted for sky diffuse radiation, dimensionless
τ_g	Relative transmittance adjusted for ground-reflected radiation, dimensionless
υ_H	Mass volume fraction of hydrogen under the pressure of ϑ_{comp}, kg/m^3

1. Introduction

One of the greatest challenges faced by today's energy transition, from an energy mix heavily relying on fossil fuels to one that is predominated by renewables, is taming the variability and uncertainty of wind and solar power generation [1]. On this point, it has been defined that if an energy system can, from a planned capacity viewpoint, fulfill load demand on a 24/365 basis with 100% certainty, that energy system is said to be *firm* [2]. Traditional coal-fired thermal power plants are firm, because they could, after proper unit commitment and generation scheduling, deliver the set amount of power, provided that the load demand level does not fall too far below their nominal capacity. As such, those plants are regarded as *dispatchable*. The question of concern, therefore, is how to firm up the variable and uncertain wind and solar power generation and make it dispatchable.

There have already been several well-known strategies that can help realize the novel idea of "dispatchable solar/wind." First and foremost is energy storage, which stores the excess energy during production peaks and releases the stored energy during times of energy deficits [3]. Another strategy is performing the coordinated operation/aggregation of spatially distributed renewable energy systems (e.g., virtual power plants), such that the variability of their joint output is milder than that of individual systems—an effect known as geographical smoothing and/or generation blending [4]. Thirdly, demand response of various kinds could help shift the load peaks to valleys, thereby obtaining a flatter load profile that is easier to manage [5]. These technologies, including energy storage, geographical smoothing, and demand response, could be collectively gathered under the umbrella term of *firm power enablers* [6].

Just very recently, a new yet counter-intuitive firm power enabler has been formally proposed, namely, *overbuilding & proactive curtailment* [2]. The core idea of overbuilding & proactive curtailment is to strategically expand the installed capacity of solar/wind power plants, such that the generation profile is sufficiently elevated for the smaller generation dips due to resource fluctuations to still exceed the load profile. This idea is certainly attractive if cost is not a concern—excessive generation often implies curtailment, which has hitherto been regarded as a sign of inefficiency and energy wastage [7]. Hence, the underlying problem is one of optimization: How much overbuilding is needed, and how to optimally combine overbuilding & proactive curtailment with other firm power enablers such that the overall cost-effectiveness of the multi-energy system is the highest?

Since the initial conception of such an optimization problem was put forth, the idea rapidly gained traction, and has led to a series of works investigating the solutions, under a variety of market settings and renewable resource regimes, including the United States [8], Italy [9], and Northern China [10]. In fact, most of these works were conducted with the International Energy Agency (IEA) Photovoltaic Power Systems Programme Task 16, which centers on the crucial aspect of firm power generation for transitioning grid-connected solar power from a marginal role to a dominant and economically core source. Interest readers are referred to the corresponding IEA report [11], as well as the recent review paper prepared by the task members [12]. The consensus of all previous studies is two-fold: (1) no single firm power enabler is able to achieve by itself firm generation cost-effectively, and (2) overbuilding & proactive curtailment plays a key role in minimizing the firm generation cost. A technical term that gauges the cost-effectiveness of firm power generation is *firm kWh premium*, which is the cost multiplier to achieve firm generation with respect to the cost of unconstrained renewable generation. (By "unconstrained," it refers to the current way of injecting power from renewables into the grid without factoring the various firm power enablers.)

Although overbuilding & proactive curtailment is, now, confirmed to be able to help achieve the lowest-cost firm generation, there has not been much formal argument or thought put into the utilization of the curtailed part of energy. Clearly, reasonable utilization of such energy would be further boost the energy economics of the system. However, because the curtailed power is highly variable and intermittent, of which the severity almost surely exceeds that of the unconstrained power from renewables, such power is unsuitable for every task that demands electricity. It is clear that a prerequisite to use the curtailed power is that the task of interest does not require a constant power supply, and can start up and shut down frequently. Therefore, this work advocates harnessing curtailed electricity for hydrogen production at the plant level. Although the majority of the previous investigations regarding firm solar power, with the exception of [10], are conducted on the system scale, undertaking the analysis at the plant level also holds fascination, which may be the case of meeting the off-shore load on an isolated island. Other potential applications of curtailed electricity include irrigation, pumped hydro storage, and many others, but they are not conceptually different from hydrogen production. This work is therefore generalizable to other applications.

As mentioned earlier, configuring a firm generation energy system requires mathematical optimization. Put it simply, given a load profile, one is tasked to optimize the sizing of solar/wind plants, the installed capacity of energy storage, as well as the hour-by-hour actions of these system constituents such that the load can be entirely satisfied. On this point, if hydrogen production is to be incorporated into the system, it necessarily implies a new formulation of the optimization problem, which is what this work is primarily concerned about. It must be noted that the configuration of the hydrogen production system in this work differs from most of the previous works [e.g., 13–15]. In most previous works, the objective function often involves just the economics of the hydrogen production system itself, such as the capital expenditure (CapEx) and operating expense (OpEx) of the system, the hydrogen and electricity sales revenue, or the environmental benefits. In this work, the objective is in regard to the joint cost and revenue structure of the firm power plant, which is more complex. The same can be said for constraints. To summarize, the first contribution of this work is to propose an optimization model that can jointly handle the configuration of a firm power plant and a hydrogen production system.

In fact, the difficulty of a mathematical optimization problem perpetually lies largely on whether the formulation can be solved using techniques that already exist. Stated differently, developing new mathematical optimization can be demanding and is often seen as a topic beyond the skill set of power system engineers; therefore, a vast majority of works involving the configuration of energy systems rely on existing solvers, such as Cplex [e.g., 16] or Gurobi [e.g., 17]. To make optimization problems compatible with existing solvers, it is commonplace to make assumptions and/or employ simplifications of various sorts during the problem setup, which makes the designed systems deviate from reality. On the other hand, it has also been frequently shown that realistic modeling of energy components, such as that for the photovoltaic (PV) system [18], battery storage [19], or hydrogen system [20], can introduce bilinear and nonlinear terms (see Section 2 for details). Hence, if such realistic models are to be used, new algorithms for solving such optimization problems are needed, which constitutes the second main contribution of this work—the refined modeling of the system's main components is introduced and a new algorithm that combines particle swarm optimization (PSO) and the branch-and-bound method is proposed.

The remaining part of the paper is organized as follows. Section 2 details the modeling of constituents of a PV–battery–hydrogen hybrid system. For each main constituent, that is, the PV system, battery storage, and the electrolyzer, two models are presented, one conventional (i.e., simplified) and the other refined; this aims at studying the implications on the final configuration when using better modeling techniques. Section 3 outlines the optimization model itself, which contains both the objective function and various operating & power balance constraints. Given the fact that the problem at hand is no longer a mixed integer linear program (MILP), standard solutions cannot be applied, a PSO–branch-and-bound hybrid algorithm that can efficiently handle the targeted optimization is proposed in the same section. Section 4 leads into the empirical part of the paper, in that, it first introduces the dataset supporting the demonstration, which contains both the electric load information and the corresponding weather information from the typical meteorological year (TMY). Various parameters and specifications required by the optimization are also solicited and set, after searching the latest reference and information from credible sources. Section 5 presents the result and discussion on four accounts: (1) differences between generic versus refined modeling, (2) cost benefits of using overbuilding & proactive curtailment, (3) sensitivity analysis on PV and battery costs, and (4) sensitivity analysis on electrolyzer costs. Conclusions follow at the end. In summary, Figure 1 provides a graphical depiction of the methodological framework of this work.

2. Modeling of the PV–battery–hydrogen hybrid system

This section proceeds with a general overview of the structure of the PV–battery–hydrogen (PBH) hybrid system. After that, the modeling of the operations of the system's main constituents is detailed. As mentioned in the introduction, one of the main aims of this work is to evaluate the implications of model realism on the eventual system configuration. As such, each of the main constituents, which include the PV array, battery storage, and electrolyzer, is modeled in two ways, one generic and one refined.

2.1. Structure of the PV–battery–hydrogen hybrid system

Figure 2 depicts the schematic diagram of the PBH system of concern, in which the PV plant and the battery storage jointly provide the electricity required by the hydrogen production system and the electric load. First, it should be noted that, differing from conventional/unconstrained PV plants, firm PV plants must be deployed together with battery storage, as well as a flexible control system, which controls the charging and discharging of the battery

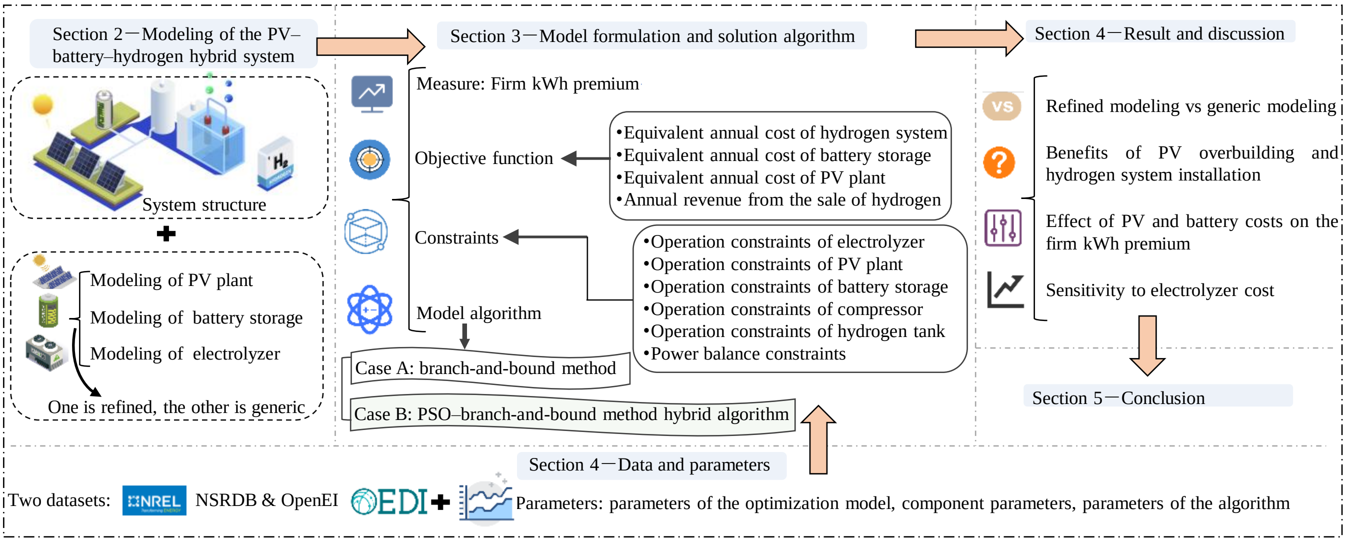

Fig. 1. The structure of this work.

storage. Battery storage preserves the excess solar energy during periods with high PV output and releases the stored energy to make up for the energy deficit during periods with low or no PV output. The coordinated scheduling of firm PV plants ensures that load demand can be met with 100% certainty. Another important trait of firm PV plants is PV oversizing, which is also absolutely necessary, because the overall cost-effectiveness of firm PV plants can only be maximized with PV oversizing, even if PV oversizing necessitates curtailment. All these ideas have been delivered and justified several times in previous works on firm power, as well as in the introduction of this work.

What separates the current work from the previous ones is that the hybrid system herein also includes a hydrogen production system. The hydrogen production system converts electricity to hydrogen. As such, it can utilize the curtailed electricity from the firm PV plant, thereby further elevating the energy economics of the hybrid system. Stated differently, the configuration of the hydrogen production system introduces a new source of revenue through the sale of hydrogen. On the other hand, hydrogen may also be perceived as a seasonal storage, facilitating the production of e-fuels through the process of electricity–hydrogen–electricity conversion, which is essential for the transition towards a 100% renewable energy system led by solar energy. Specifically, these e-fuels can be fed into the thermoelectric generators to generate electricity during periods when PV power falls below the requirement of load. Although the cost-effective advantages of harnessing hydrogen as seasonal storage have been substantiated, this aspect is not taken into consideration herein for two reasons: (1) The firm PV plant already satisfies electric demand at all times, and (2) the conversion efficiency of electricity–hydrogen–electricity conversion is low. Therefore, the hydrogen production system is tasked to provide an intermediate product and raw material for the chemical industry, encompassing the synthesis of ammonia, methanol, or hydrogenation reactions in petroleum refining processes; the purpose of this work is to assess whether hydrogen production presents an economic benefit.

Within the hydrogen production system there are three components, namely, the electrolyzer, compressor, and hydrogen tank, among which the electrolyzer requires the most attention for its working mechanism is the most complex. The low-pressure hydrogen, which is produced by the electrolyzer with the input of the nearly zero-cost curtailed electricity from the firm PV plant, is compressed into high-pressure hydrogen, which is then stored in the hydrogen tank. In this work, it is assumed that the hydrogen in the tank is sold to local hydrogen wholesalers at 12:00 midnight each day. In the following three subsections, the modeling of the PV plant, battery storage, and electrolyzer are formulated in two ways.

2.2. *Modeling of PV plant*

In what follows, the generic PV plant model is referred to as model A, and the refined PV plant model as model B.

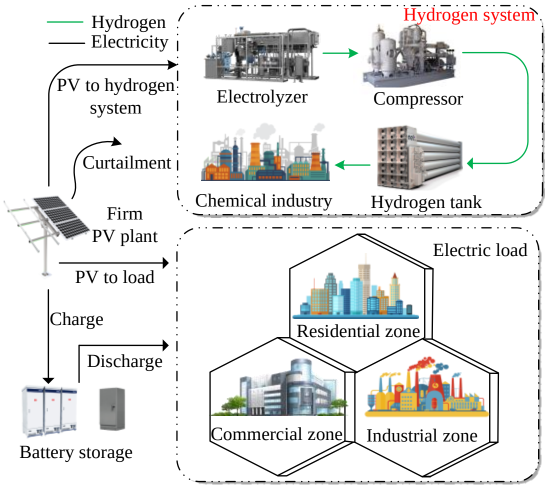

Fig. 2. A firm PV plant equipped with battery storage and hydrogen production system.

2.2.1. Generic PV plant model A

For new or planned PV plants where long-term PV measurements are absent, one is still able to estimate its power output through simulation [21]; this is in fact a necessary step in solar resource assessment and bankability analysis [22, 23]. Modeling a PV plant requires two groups of information. One of those is a set of meteorological variables, including global horizontal irradiance (GHI), ambient temperature, wind speed, or sometimes, the ground albedo. These variables should span, or be able to represent, a long enough time period, such that they can typify the local weather regime. The other set of information is related to the design parameters of the plant, which include but are not limited to panel orientation, panel model, panel layout, and inverter model. Conventionally, since PV generation plays just a marginal role in the whole energy mix, power system engineers usually employ simplified PV modeling to estimate PV power output.

Indeed, the conventional (i.e., generic) PV plant model is very simple, as it only requires three equations [14]:

$$G_c = B_n \cos\theta + D_h \frac{1+\cos S}{2} + \rho G_h \frac{1-\cos S}{2}, \tag{1}$$

$$T_{\text{cell}} = T_{\text{amb}} + \left(T_{\text{mod}}^{\text{NOCT}} - 20^{\circ}\text{C}\right) \frac{G_c}{800\ \text{W/m}^2}, \tag{2}$$

$$P_{\text{pv}} = \left[1 + \gamma_{\text{mod}} \left(T_{\text{cell}} - 25^{\circ}\text{C}\right)\right] \frac{\eta_{\text{inv}}^{\text{norm}} \widetilde{P}_s G_c}{1000\,\text{W/m}^2}. \tag{3}$$

Equation (1) is known as the *isotropic transposition equation*, which converts the horizontal irradiance components to that on the tilted surface, while assuming isotropic sky- and ground-view factors. In Eq. (1), G_c, B_n, D_h, and G_h are global tilted irradiance (GTI), beam normal irradiance (BNI), diffuse horizontal irradiance (DHI), and GHI, respectively; S is the tilt angle of the PV array; θ is the incidence angle, which can be calculated via solar positioning; and ρ is the foreground albedo, which may be assumed to be 0.2 for non-bright surfaces. Equation (2) converts the GTI (G_c) and ambient temperature (T_{amb}) into cell temperature (T_{cell}). In this equation, $T_{\text{mod}}^{\text{NOCT}}$ is the nominal operating cell temperature of PV modules, which is usually known. Lastly, Eq. (3) uses the information attained thus far to model the AC power output of the PV system (P_{pv}). In Eq. (3), $\widetilde{P}_s$ is the rated power of the PV plant; γ_{mod} is the temperature coefficient of the PV module, which is known from the manufacturer; and $\eta_{\text{inv}}^{\text{norm}}$ is the nominal efficiency of the inverter. It is worth mentioning that Eqs. (1–3) can be applied to compute the PV output during any time t, thus the subscript t is omitted here for notation brevity, and likewise for the subsequent PV model B.

2.2.2. Refined PV plant model B

Conventional PV model A is overly idealistic owing to its crude modeling of the conversion process, which may result in large deviations between the simulated and actual PV output [24]. Therefore, the refined PV modeling strategy, which is known as *model chain*, is now being increasingly valued. Model chain utilizes a collection of energy meteorology models in cascade, where the output of a preceding model is used as the input of the succeeding one. A typical model chain is shown in Fig. 3. It should be highlighted that the complexity of a "full" model chain goes beyond that depicted in Fig. 3, and the reader is referred to Chapter 11 of the book by Yang and Kleissl [25] for a complete tutorial. Nonetheless, the model chain in Fig. 3 is already sufficient for most applications. In the following, the basic principle of each component model in the chain, according to Fig. 3, is briefly described.

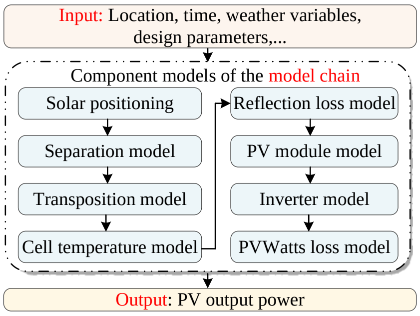

Fig. 3. Illustration of a typical model chain, which includes eight component models.

To fully describe the position of the sun, as observed from the titled PV panel surface, three angles, namely, the solar azimuth angle (α), solar zenith angle (Z), and incidence angle (θ), are required. These angles can be computed via solar positioning, as long as the location and time are known. Solar position algorithms have performance conflicts in terms of accuracy and computation time [26]. For the current simulation, time is not a main concern. Therefore, the algorithm developed by Reda and Andreas [27], which has the highest accuracy, is herein selected.

With a separation model, DHI and BNI can be obtained from GHI. Inherently, these three components adhere to the *closure relationship*, that is:

$$G_h = B_n \cos Z + D_h. \tag{4}$$

In the literature, a multitude of separation models exist, each diverging from one another in terms of model performance and formulation [see 28, 29, for reviews]. Since the meteorological data of a particular location, which can be acquired from the National Solar Radiation Database (NSRDB) [30, 31], already encompasses BNI, DHI, and GHI, the need for separation modeling is circumvented in this work. However, what is worth noting is that the NSRDB uses the DISC separation model [32] to split DHI and BNI from GHI under cloudy skies, and uses the REST2 clear-sky model to [33] directly compute all three irradiance components under clear skies.

The function of a transposition model, as mentioned earlier, is to convert BNI, DHI, and GHI into GTI via [34]:

$$G_c = B_n \cos\theta + R_d D_h + \rho R_r G_h, \tag{5}$$

where R_d is the sky-view factor or the diffuse transposition factor; $R_r = (1 - \cos S)/2$ is the ground-view factor or transposition factor due to ground reflection, which is usually assumed to be isotropic. Therefore, only R_d is unknown and needs to be modeled. Indeed, the modeling of R_d is the sole element distinguishing various transposition models. When the sky is assumed to be isotropic, $R_d = (1 + \cos S)/2$, in which case Eq. (5) is reduced to Eq. (1). In this work, the quasi-universal Perez model [35] is utilized to determine the value of R_d, due to its well-tested accuracy and reliability in comparison with other alternatives [see 34, for a comparison study].

Though the GTI holds the foremost influence over PV output, the next important factor is the cell temperature. In most occasions, the cell temperature is governed by GTI, wind speed (V), and ambient temperature. Similar to the case of separation and transposition models, many options are available for estimating the cell temperature. Here, the empirical Sandia Array Performance Model (SAPM), as documented in [36], is considered without loss of generality, and it takes the form:

$$T_{\text{mod}} = G_c \exp(p + qV) + T_{\text{amb}}, \tag{6}$$

$$T_{\text{cell}} = T_{\text{mod}} + \frac{G_c}{1000\text{W/m}^2}\Delta T, \tag{7}$$

where T_{mod} is the module temperature; p, q, and ΔT are model parameters having to do with the encapsulation and mounting of the modules, which can be solicited from a look-up table. It should be emphasized that the unit of G_c in Eq. (6) is W/m^2, and V represents the wind speed with a unit of m/s at a height of 10 m.

When light strikes the glass or other encapsulation materials, it results in a reflection loss, which lowers the PV output. Three relative transmittances (τ_b, τ_d, and τ_g) are usually adopted to account for the respective losses in the three components of GTI. Upon incorporating reflection losses, the GTI is transformed into the effective irradiance (G_c'), which can be denoted by the following equation:

$$G_c' = \tau_b B_n \cos\theta + \tau_d R_d D_h + \tau_g \rho R_r G_h. \tag{8}$$

Again, numerous reflection loss models have been proposed to estimate τ_b, τ_d, and τ_g. In this work, the value of τ_b is determined using the Fresnel equation [37], whereas the values of τ_d and τ_g are determined based on the analytical expressions derived by Xie et al. [38].

DC models, or PV models, as the name suggests, calculate the DC power (P_{dc}); they can be broadly grouped into two categories: empirical models and equivalent-circuit-based physical models. The latter is capable of acquiring the entire I–V curve of the PV plant, but detailed design parameters of the system, such as the panel layout or connection, are necessary. In contrast, empirical models demand only a few fundamental parameters to be known. In this work, the widely-used empirical PVWatts model [39] is leveraged to estimate the DC power, which is formulated as follows:

$$P_{\text{dc}} = \left[1 + \gamma_{\text{mod}} \left(T_{\text{cell}} - 25°\text{C}\right)\right] \frac{\widetilde{P}_s G_c'}{1000 \text{ W/m}^2}. \tag{9}$$

To fulfill the load demand, DC power must be passed through some power electronics to become AC power (P_{ac}); this process may be represented in a surrogate fashion by an inverter model. The DC–AC conversion follows the PVWatts inverter model [39], which accounts for inverter clipping; it is:

$$\eta_{\text{inv}} = \frac{\eta_{\text{inv}}^{\text{norm}}}{0.9637}\left(-0.0162\frac{P_{\text{dc}}\eta_{\text{inv}}^{\text{norm}}}{\widetilde{P}_{\text{ac}}} - 0.0059\frac{\widetilde{P}_{\text{ac}}}{P_{\text{dc}}\eta_{\text{inv}}^{\text{norm}}} + 0.9858\right), \tag{10}$$

$$P_{\text{ac}} = \min\left(\eta_{\text{inv}} P_{\text{dc}}, \widetilde{P}_{\text{ac}}\right), \tag{11}$$

where $\widetilde{P}_{\text{ac}}$ is the rated output power of the inverter, η_{inv} is the time-varying inverter efficiency.

Through the component models mentioned thus far, the AC power under various meteorological conditions can already be estimated to a fairly accurate degree. However, for a more realistic simulation of the PV output, it is crucial to account for additional losses, such as wiring loss or soiling loss. Accurate modeling of the losses also needs detailed information about the PV plant, which is more often than not unknown. To that end, the PVWatts loss model [39], which simply considers various losses in percentage forms, is selected to roughly estimate these losses.

2.3. Modeling of battery storage

PV plants output no or little power under overcast skies and at night, and the PBH hybrid system must rely upon energy stored during the day to satisfy the energy demand during those periods. Similar to the case of PV, two battery models are outlined in this subsection, one generic battery model (or model A) and one refined battery model (or model B).

2.3.1. *Generic battery model A*

Because the energy available in batteries over the next hour depends on the state of power of the current hour, as well as the charging/discharging operation, the main governing equations of battery models must contain a notion of time. The generic battery model, which is widely employed by the energy sector [40], is as follows:

$$E_{b,t+1} = (1 - \sigma_b)E_{b,t} + \Delta t\left(\eta_{\mathrm{ch}}^{\mathrm{ref}} P_{\mathrm{ch},t} - \frac{P_{\mathrm{dis},t}}{\eta_{\mathrm{dis}}^{\mathrm{ref}}}\right), \tag{12}$$

where $E_{b,1}$, $E_{b,t}$, and $E_{b,t+1}$ represent the electrical energy stored in the battery storage at time $t = 1$, t, and $t+1$, respectively; Δt is the time interval, which is 1 h in this work; $P_{\mathrm{ch},t}$ and $P_{\mathrm{dis},t}$ indicate the charging power and discharging power of battery storage at time t, respectively; σ_b is the self-discharge rate; $\eta_{\mathrm{ch}}^{\mathrm{ref}}$ and $\eta_{\mathrm{dis}}^{\mathrm{ref}}$ are charging and discharging efficiencies.

Although Eq. (12) is self-explanatory, one has to note that several constraints ought to be met to reflect the reality. The basic ones are:

$$0 \le P_{\mathrm{ch},t} \le B_{\mathrm{ch},t}\widetilde{P}_{\mathrm{ch}}, \tag{13}$$

$$0 \le P_{\mathrm{dis},t} \le B_{\mathrm{dis},t}\widetilde{P}_{\mathrm{dis}}, \tag{14}$$

$$B_{\mathrm{ch},t} + B_{\mathrm{dis},t} \le 1, \tag{15}$$

$$0 \le E_{b,t} \le S_b, \tag{16}$$

$$E_{b,1} = 0.8 S_b. \tag{17}$$

Constraints (13) and (14) suggest that the charging and discharging powers cannot exceed their physical limits, which are narrated by the pre-defined upper limits of the charging ($\widetilde{P}_{\mathrm{ch}}$) and discharging ($\widetilde{P}_{\mathrm{dis}}$) powers. Additionally, these upper limits should be multiplied with $B_{\mathrm{ch},t}$ and $B_{\mathrm{dis},t}$, which are binary variables indicating the battery charging and discharging states. Constraint (15) prevents simultaneous charging and discharging of battery storage over the same time period. Constraint (16) states that the energy stored at any time t should neither exceed the rated capacity (S_b) nor fall below 0. The initial (i.e., $t = 1$) energy available in the battery storage is set to be 0.8 times the rated capacity, see Eq. (17).

2.3.2. *Refined battery model B*

The generic battery model A treats the charging/discharging efficiencies and the upper limits of the charging/discharging power of battery storage as constants, implying their independence from the state of charge (SoC) of battery storage [41, 42]. Since the decoupling among the SoC, efficiencies, and upper power limits of battery storage fails to provide an accurate representation of the actual operating mechanism of batteries, the real operational behaviors of battery storage may deviate from the scheduling plan. Accordingly, a measurement-based battery model, which was developed by Gonzalez-Castellanos et al. [19], is used in this work to describe the interaction among these three variables.

Prior to elaborating further on this refined battery model, it is thought appropriate to elaborate first on the meaning of some symbols. $P_{\mathrm{in},t}$ and $P_{\mathrm{out},t}$ are the power that enters/leaves battery storage at time t before/after the battery efficiencies have been considered, respectively; SoC_t is the SoC of battery storage at time t; the set $\mathcal{I}$ and vector $(\widehat{\mathrm{SoC}}_{\mathrm{ch},i}, \widehat{P}_{\mathrm{ch},i}, \widehat{P}_{\mathrm{in},i}), i \in \mathcal{I}$ are respectively the battery charging measurement set and its i^{th} 3-dimensional charging measurement point; the set $\mathcal{O}$ and vector $(\widehat{\mathrm{SoC}}_{\mathrm{dis},o}, \widehat{P}_{\mathrm{dis},o}, \widehat{P}_{\mathrm{out},o}), o \in \mathcal{O}$ are respectively the battery discharging measurement set and its o^{th} 3-dimensional discharging measurement point. The core concept of this battery model revolves around the use of the two measurement sets, namely, $\mathcal{I}$ and $\mathcal{O}$, to define the feasibility region of battery operations. To put it simply, any battery discharging point $(\mathrm{SoC}_t, P_{\mathrm{dis},t}, P_{\mathrm{out},t})$ can be expressed as a convex combination of battery discharging measurements, as demonstrated in Fig. 4; similarly, any battery charging point $(\mathrm{SoC}_t, P_{\mathrm{ch},t}, P_{\mathrm{in},t})$ can be mathematically written as a convex combination of battery charging measurements.

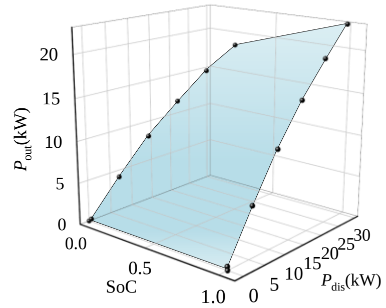

Fig. 4. The feasibility region (light blue area) for battery discharging points, which is written as a convex combination of 14 battery discharging measurement points (black dots). These measurements were acquired from battery storage with a rated capacity of 5.32 kWh [19].

The measurement-based (i.e., refined) battery model, which includes Eqs. (16) and (17), can be formulated as

$$E_{b,t+1} = E_{b,t} + P_{\text{in},t}\Delta t - P_{\text{out},t}\Delta t, \tag{18}$$

$$P_{\text{in},t} = \sum_{i\in\mathcal{I}} x_{i,t} N_b \widehat{P}_{\text{in},i}, \tag{19}$$

$$P_{\text{ch},t} = \sum_{i\in\mathcal{I}} x_{i,t} N_b \widehat{P}_{\text{ch},i}, \tag{20}$$

$$\text{SoC}_t = \sum_{i\in\mathcal{I}} x_{i,t} \widehat{\text{SoC}}_{\text{ch},i} + \sum_{o\in\mathcal{O}} x_{o,t} \widehat{\text{SoC}}_{\text{dis},o}, \tag{21}$$

$$\sum_{i\in\mathcal{I}} x_{i,t} = 1,\ 0 \le x_{i,t} \le 1, \tag{22}$$

$$P_{\text{out},t} = \sum_{o\in\mathcal{O}} x_{o,t} N_b \widehat{P}_{\text{out},o}, \tag{23}$$

$$P_{\text{dis},t} = \sum_{o\in\mathcal{O}} x_{o,t} N_b \widehat{P}_{\text{dis},o}, \tag{24}$$

$$\sum_{o\in\mathcal{O}} x_{o,t} = 1,\ 0 \le x_{o,t} \le 1, \tag{25}$$

$$E_{b,t} = \text{SoC}_t S_b, \tag{26}$$

$$S_b = N_b S_{b,\text{ref}}, \tag{27}$$

$$0 \le N_b \le \overline{N}_b, \tag{28}$$

where $x_{i,t}$ is the weight associated with the i^{th} battery charging measurement point; $x_{o,t}$ is the weight associated with the o^{th} battery discharging measurement point; $S_{b,\text{ref}}$ is the rated capacity of the testing battery from which the charging and discharging measurements were acquired; N_b commonly denotes the integer number of batteries configured in the hybrid system; $\overline{N}_b$ is the maximum value allowed for N_b. It should be emphasized that when $S_{b,\text{ref}}$ is sufficiently small, relaxing the integer variable N_b to a real variable only introduces negligible errors [43]. Hence, to improve the computational efficiency of the optimization model embedded with this battery model, the value of N_b should be relaxed as far as possible to be a positive real number. In fact, the technique of variable relaxation is utilized in this work.

The hidden information in the battery charging and discharging measurements can be captured and exploited to constrain the working patterns of battery storage, which are the main features that distinguish this refined battery model B from the generic battery model A. Specifically, Eqs. (19)–(25) use the battery charging/discharging measurements to limit the values of the battery charging/discharging points, which reflects the interdependence of the SoC and charging/discharging power of battery storage. Furthermore, the time-varying battery charging efficiency ($\eta_{\text{ch},t}$) and discharging efficiency ($\eta_{\text{dis},t}$) are implicitly considered, as there exist definitions of $\eta_{\text{ch},t} = P_{\text{in},t}/P_{\text{ch},t}$ and

$\eta_{\text{dis},t} = P_{\text{dis},t}/P_{\text{out},t}$. Next, the description of the remaining constraints on this model is presented. As shown in Eq. (18), the available energy of battery storage at time $t + 1$ is strictly equal to the stored energy at time t minus the power fed into the battery times the time interval, while the power output from the battery times the time interval is added. Constraint (26) reveals the relation between the SoC and the available energy of battery storage during each time. The energy storage configured in the hybrid system can be perceived as composed of N_b test batteries, as indicated by Eq. (27). Constraint (28) denotes that the value of N_b is confined by its bounds.

2.4. Modeling of electrolyzer

This subsection again consists of two parts, which describe the generic electrolyzer model (or model A) and the refined electrolyzer model (or model B).

2.4.1. Generic electrolyzer model A

With the curtailed electricity from the firm PV plant as power input, water is electrolyzed into hydrogen following an electrochemical reaction process. The generic model of an electrolyzer is simplistic, as it contains only one equation with one constraint [44]:

$$D_{\text{elec},t} = \frac{\eta_{\text{elec}}^{\text{ref}} P_{\text{elec},t}}{H_h}, \tag{29}$$

$$0 \leq P_{\text{elec},t} \leq \widetilde{P}_{\text{elec}}, \tag{30}$$

where $D_{\text{elec,t}}$ and $P_{\text{elec},t}$ are the hydrogen production rate, with a unit of kg/h, and input power of the electrolyzer at time t, respectively; $\eta_{\text{elec}}^{\text{ref}}$ is the reference hydrogen production efficiency of the electrolyzer; H_h is the hydrogen high heating value, with a unit of kWh/kg; $\widetilde{P}_{\text{elec}}$ is the rated power of the electrolyzer. Equation (29) states that the hydrogen production rate of the electrolyzer depends upon the production efficiency and input power. Constraint (30) envelopes the input power between the rated value and zero.

2.4.2. Refined electrolyzer model B

The generic electrolyzer model A assumes that the hydrogen production efficiency is constant. However, in practice, the load ratio of an electrolyzer, which is defined as the ratio of the input power to the rated power, impacts its hydrogen production efficiency. Neglecting the dynamic characteristics of the hydrogen production efficiency undermines the accuracy of modeling, thus a refined electrolyzer model B proposed by Jiang et al. [20], which incorporates the interplay between the load ratio of the electrolyzer and the hydrogen production efficiency, is considered in this work. The remainder of this subsection details the process of constructing this electrolyzer model, along with its transformation into a tractable model using the piecewise linear approach. Note that the subscript t has been removed from the variables here, as in Section 2.2, for notation brevity.

Since the electrolyte cell is the basic unit where the electrochemical reaction takes place within electrolyzers, the cell efficiency (η_{cell}), which is the product of the current efficiency (η_I) and voltage efficiency (η_U) of an electrolyte cell, may be used as a proxy for the time-varying hydrogen production efficiency of the electrolyzer (η_{elec}) [45], as specified below:

$$\eta_{\text{elec}} \approx \eta_{\text{cell}} = \eta_I \eta_U. \tag{31}$$

The current efficiency of an electrolyte cell is commonly defined as [46]:

$$\eta_I = 1 - \frac{I_{\text{loss}}}{I} = 1 - \frac{I_{\text{loss}}}{iA}, \tag{32}$$

where i and I are respectively the current density and current flowing through the electrolyte cell; A is the cross-sectional area of an electrolyte cell; and I_{loss} is the loss current. According to Fick's law and Faraday's law, the loss current of an electrolyte cell can be computed as [47, 48]:

$$I_{\text{loss}} = 2\,A\,F\,D_H\,S_H \Delta P/e_M, \tag{33}$$

where F is the Faraday constant; D_H and S_H are the hydrogen diffusivity coefficient and hydrogen solubility coefficient under the operating temperature (T_0); ΔP is the pressure difference across the electrolyzer membrane, and e_M is the average membrane thickness. In general, the membrane thickness gradually thins due to the physical or chemical aging of an electrolyzer. From a simplified viewpoint, the membrane thickness at the half-life of an electrolyzer is chosen in this work as a representation of the average membrane thickness.

The definition of the voltage efficiency (η_U) of an electrolyte cell—-note that the computation of η_U in the refined electrolyzer model proposed by Jiang et al. [20] is erroneous and necessitates correction in accordance with [46]—is given by the ratio of the reversible cell voltage to the operating cell voltage:

$$\eta_U = \frac{U_{\text{rev}}}{U_{\text{cell}}} = \frac{U_{\text{rev}}}{U_{\text{rev}} + U_A + U_C + IR_0} \approx \frac{U_{\text{rev}}}{U_{\text{rev}} + U_A + IR_0}, \tag{34}$$

with

$$U_{\text{rev}} = 1.5184 - 1.5452 \times 10^{-3} \times T_0 + 9.523 \times 10^{-5} \times T_0 \times \ln(T) + 9.84 \times 10^{-8} \times T_0^2, \tag{35}$$

where U_{rev} denotes the reversible cell voltage, which represents the minimum cell voltage necessary for the electrolytic dissociation of one water molecule; U_{cell} is the operating cell voltage at the reaction temperature T_0, which is equal to the voltage across an electrolytic cell; U_A is the anodic over-potential; U_C is the cathodic over-potential, which is disregarded in this work due to its negligible magnitude [49]; R_0 is the ohmic resistance of an electrolyte cell. From Eq. (34), it is found that the operating cell voltage may be approximated as the sum of U_{rev}, U_A, and the potential due to ohmic loss, i.e., IR_0. The formulas for calculating the anodic over-potential and ohmic resistance of an electrolyte cell can be written as [49, 50]

$$U_A = \frac{RT_0}{\alpha_A zF} \ln\left(\frac{i}{i_{0\text{A}}\gamma_A}\right), \tag{36}$$

$$R_0 = \frac{e_M}{Ak} + \frac{e_A}{A\sigma_A} + \frac{e_C}{A\sigma_C}, \tag{37}$$

where R is the ideal gas constant; α_A is the charge transfer coefficient at the anodic side; z is the stoichiometric coefficient representing the number of exchanged electrons in the water electrolysis reaction; $i_{0\text{A}}$ and γ_A are the anodic exchange current density and the anodic rugosity factor; e_A and σ_A are the anodic current collector thickness and the conductivity of the anodic current collector; e_C and σ_C are the cathodic current collector thickness and the conductivity of the cathodic current collector; k is the average electrolyte conductivity. Similar to the average membrane thickness, the value of k pertains to the electrolyte conductivity at the half-life of the electrolyzer.

Combining Eqs. (31)–(37) yields:

$$\eta_{\text{elec}} = \left(1 - \frac{2FD_H S_H \Delta P}{ie_M}\right)\left[\frac{U_{\text{tn}}}{U_{\text{tn}} + \frac{RT_0}{\alpha_A zF}\ln\left(\frac{i}{i_{0\text{A}}\gamma_A}\right) + i\left(\frac{e_M}{k} + \frac{e_A}{\sigma_A} + \frac{e_C}{\sigma_C}\right)}\right]. \tag{38}$$

It is apparent from Eq. (38) that the hydrogen production efficiency of the electrolyzer is closely related to the current density flowing through the electrolyzer. Nevertheless, in practical operations, the load ratio emerges as a more readily available and universally applicable parameter than the current density. The load ratio (ρ_{ld}) can be calculated as:

$$\rho_{\text{ld}} = \frac{U_{\text{cell}} I}{\widetilde{U}_{\text{cell}} \widetilde{I}} = \frac{U_{\text{cell}} i}{\widetilde{U}_{\text{cell}} \widetilde{i}}, \tag{39}$$

where the tilde above a quantity denotes the rated value of that quantity. As can be seen from Eqs. (38) and (39), both the hydrogen production efficiency and load ratio show variations with respect to the current density. In other words, when provided with a dataset of current density values that span uniformly between 0 and $\widetilde{i}$, it becomes feasible to acquire two distinct sets of data representing the corresponding hydrogen production efficiency and load ratio, respectively. Moreover, by multiplying the load ratio and rated power, the electrolyzer input power can be determined; the hydrogen production rate of the electrolyzer can then be calculated based on Eq. (29) with the known hydrogen production efficiency and input power of the electrolyzer.

There is but one issue with integrating the above refined electrolyzer model B into the optimization model elaborated in Section 3, that is, the optimization model simultaneously depends on both $D_{\mathrm{elec},t}$ and $P_{\mathrm{elec},t}$, yet, the nonlinear relationship between the two quantities prevents the execution of the convex optimization routine. Fortunately, both $D_{\mathrm{elec},t}$ and $P_{\mathrm{elec},t}$ are related to the current density i. As such, by enumerating a sequence of discrete i values, a one-to-one mapping between discrete $D_{\mathrm{elec},t}$ and discrete $P_{\mathrm{elec},t}$ may be derived. Be that as it may, the optimization routine requires $D_{\mathrm{elec},t}$ and $P_{\mathrm{elec},t}$ to be continuous variables. As such, a piecewise linear fitting must be carried out, as to convert the discrete pairs of $D_{\mathrm{elec},t}$ and $P_{\mathrm{elec},t}$ into a continuous curve, portraying the relationship between continuous $D_{\mathrm{elec},t}$ and continuous $P_{\mathrm{elec},t}$. This entire fitting process is illustrated in Fig. 5.

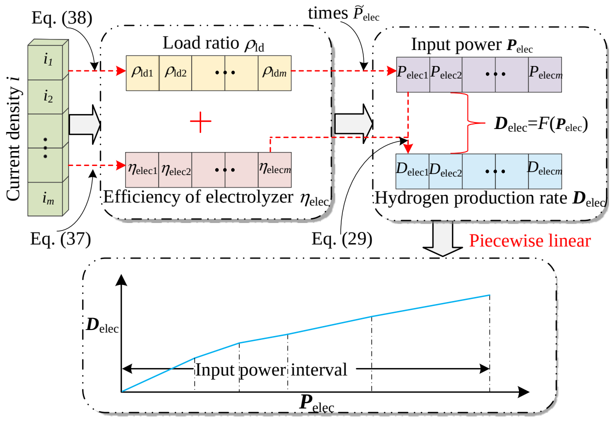

Fig. 5. An illustration of the curve fitting procedure for mapping the hydrogen production rate of the electrolyzer as a function of the input power.

More specifically, once the datasets for the hydrogen production rate and input power of the electrolyzer are obtained from the i sequence, the `pwlf-python` package [51] is used to calculate the slope, intercept, and endpoint locations of each line segment for a specified rated power and a given number of line segments. At this stage, Eq. (29) can be re-expressed as:

$$D_{\mathrm{elec},t} = \sum_{l\in\mathcal{L}} \left(a_l P_{\mathrm{elec},l,t} + b_l B_{\mathrm{elec},l,t}\right), \tag{40}$$

$$P_{\mathrm{elec},t} = \sum_{l\in\mathcal{L}} P_{\mathrm{elec},l,t}, \tag{41}$$

$$\sum_{l\in\mathcal{L}} B_{\mathrm{elec},l,t} = 1, \tag{42}$$

$$B_{\mathrm{elec},l,t} P^0_{\mathrm{elec},l} \le P_{\mathrm{elec},l,t} \le B_{\mathrm{elec},l,t} P^0_{\mathrm{elec},l+1}, \tag{43}$$

where l indexes the line segments; $\mathcal{L}$ is the set of positive integers within the specified number of line segments; a_l, b_l, $P^0_{\mathrm{elec},l}$, and $P^0_{\mathrm{elec},l+1}$ denote the slope, intercept, left endpoint, and right endpoint of the l^{th} line segment, respectively; $P_{\mathrm{elec},l,t}$ is the input power corresponding to the l^{th} line segment at time t; $B_{\mathrm{elec},l,t}$ is a binary variable representing the status of the l^{th} line segment, with a value of 1 when the input power falls within that specific line segment, and 0 otherwise. Using the piecewise linear approach, Eqs. (40) and (41) estimate the hydrogen production rate and input power of the electrolyzer. As suggested by Eq. (42), the input power during each time can only lie within one line segment. The line segment, within which the input power of the electrolyzer at time t is located, is identified by constraint (43).

3. Model formulation and solution algorithm

In this section, the measure for quantifying the *effective dispatchable* cost of PV generation is introduced, and the optimization model, which includes an objective function and numerous constraints, is formulated, so as to achieve the lowest-cost firm PV generation. Because the optimization model cannot be solved using off-the-shelf solvers (see below for more details), a new hybrid algorithm is proposed, which comprises an outer meta-heuristic loop and an inner branch-and-bound solver.

3.1. Measure of cost-effectiveness of firm PV generation

In all studies concerning the configuration of multi-energy systems, a quantifier is needed to assess the economic viability of the configured system; the present PBH hybrid system is no exception. Insofar as firm generation is concerned, the overarching measure employed in this work is known as the "firm kWh premium," which was first and formally conceptualized by Perez et al. [6]. The firm kWh premium is the ratio of the costs of firm and unconstrained PV. Because the levelized cost of electricity (LCOE) is the dominant quantifier for electricity, the firm kWh premium is based upon it, i.e.,

$$\text{Firm kWh premium} = \frac{\text{Firm PV LCOE}}{\text{Unconstrained PV LCOE}}, \tag{44}$$

where

$$\text{LCOE} = \frac{\text{Equivalent annual cost of generation}}{\text{Annual electricity production}}. \tag{45}$$

It must be highlighted that the choice of using firm kWh premium instead of using LCOE directly is because the value of the PV LCOE varies across different markets and radiation regimes. Stated differently, a cost multiplier rather than an absolute cost is able to relieve the market or radiation-regime dependency, and thus should be preferred. As demonstrated by Eq. (45), the calculation of the PV LCOE involves the equivalent annual cost of generation—the word "equivalent" suggests the conversion of the total cost of each component to a one-year equivalent value considering the component lifetime, see Eq. (47)—and the annual electricity production.

Note that there are several caveats when using Eq. (45). The equivalent annual cost of unconstrained PV only includes the equivalent annual investment cost, or the "CapEx," and the equivalent annual operation and maintenance (O&M) cost, or the "OpEx," of that unconstrained PV plant. However, for firm PV, its cost also embeds the CapEx and OpEx of the firm power enablers, such as battery storage or the overbuilt part of PV. In addition, considering the present PBH hybrid system, the annual hydrogen sale revenue, as well as the CapEx and OpEx of the hydrogen system, should also be incorporated into the objective function. Regarding the annual electricity production, in the case of unconstrained PV plants, it refers to the annual energy yield. Nonetheless, because firm PV is tasked to, and in fact can, satisfy the load demand with 100% certainty, its generation must be equal to the load demand. Based on Eqs. (44) and (45), the firm kWh premium involves four LOCE terms, and three of them are constants for a given set of data (i.e., load condition, weather condition, and unconstrained PV system design), with the only adjustable component being the equivalent annual cost of a PBH hybrid system, which is therefore used as the objective function of the optimization model.

3.2. Objective function

The objective function of the optimization model can be described as

$$\begin{aligned}
\underset{S_b, P_{\mathrm{ch},t}, X_s, \widetilde{P}_{\mathrm{elec}}, \widetilde{P}_{\mathrm{comp}}, \widetilde{S}_{\mathrm{tank}}, D_H^t}{\operatorname{argmin}} \Bigg\{ & c_b S_b \left(\xi_b + l_b \sum_{t \in \mathcal{T}} \frac{P_{\mathrm{ch},t}}{S_b} \right) + c_s X_s \widetilde{P}_s \left(\xi_s + l_s \right) \\
& + c_{\mathrm{elec}} \widetilde{P}_{\mathrm{elec}} \left(\xi_{\mathrm{elec}} + l_{\mathrm{elec}} \right) + c_{\mathrm{comp}} \widetilde{P}_{\mathrm{comp}} \left(\xi_{\mathrm{comp}} + l_{\mathrm{comp}} \right) \\
& + c_{\mathrm{tank}} \widetilde{S}_{\mathrm{tank}} \left(\xi_{\mathrm{tank}} + l_{\mathrm{tank}} \right) - \sum_{t \in \mathcal{T}} \Delta t \lambda_H D_{H,t} \Bigg\},
\end{aligned} \tag{46}$$

with

$$\xi_y = \frac{\tau_0(1+\tau_0)^{T_y}}{(1+\tau_0)^{T_y}-1}, \quad y \in \mathcal{Y} = \{b,\ s,\ \text{elec},\ \text{comp},\ \text{tank}\}, \tag{47}$$

where y indexes the energy components configured in the hybrid system; $\mathcal{T}$ and $\mathcal{Y}$ are the sets of time stamps and energy components; subscripts b, s, elec, comp, and tank stand for the quantities related to the battery storage, solar PV, electrolyzer, compressor, and hydrogen tank, respectively; parameters c, ξ, l, and T are the unit investment cost, capital recovery factor, OpEx factor, and lifetime of the corresponding component, respectively; X_s is the oversizing ratio of the PV plant; $\widetilde{P}_{\text{comp}}$ is the rated power of the compressor; $\widetilde{S}_{\text{tank}}$ is the rated capacity of the tank; λ_H is the hydrogen sale price in \$/kg; $D_{H,t}$ is the volume of hydrogen for sale at time t; and τ_0 is the discount rate.

The first five terms of the objective function signify, in order, the equivalent annual cost of battery storage, PV, electrolyzer, compressor, and hydrogen tank, whereas the last term represents the annual revenue from the sale of hydrogen. Particularly, the factor method [52] is utilized to determine the OpEx of the PV plant, electrolyzer, compressor, and hydrogen tank, and the OpEx of battery storage is estimated from its discharging power following the common practice [53]. As for Eq. (47), it indicates that the capital recovery factor of each component can be computed based on the discount rate and the lifetime of the corresponding component.

3.3. Constraints

During operation, neither the operation constraints of each component nor the power balance constraint should be violated. The operation constraints for battery storage are given in constraints (12)–(17) or constraints (16)–(28), depending on whether the generic or refined battery model is selected; the operation constraints of the electrolyzer are given in constraints (29)–(30) or constraints (40)–(43), depending on whether the generic or refined electrolyzer model is selected. Besides these, other necessary constraints are elaborated next.

3.3.1. Operation constraints of compressor

The function of a compressor is to reduce the volume of hydrogen by turning low-pressure hydrogen into high-pressure hydrogen for easy storage in the hydrogen tank, which is often subject to space restrictions. The operation constraints of a compressor are expressed as follows [54]:

$$P_{\text{comp},t} = p_{\text{comp}}^{\text{ref}} D_{\text{elec},t} \frac{\ln\left(\vartheta_{\text{comp}}/\vartheta_0\right)}{\ln\left(\vartheta_{\text{comp}}^{\text{ref}}/\vartheta_0\right)}, \tag{48}$$

$$0 \le P_{\text{comp},t} \le \widetilde{P}_{\text{comp}}, \tag{49}$$

where $P_{\text{comp},t}$ is the input power of the compressor at time t; $p_{\text{comp}}^{\text{ref}}$ represents the hourly energy consumption of the compressor when compressing 1 kg of hydrogen under the standard working pressure of the compressor ($\vartheta_{\text{comp}}^{\text{ref}}$); ϑ_0 is the standard atmospheric pressure in bar units; and ϑ_{comp} is the normal working pressure of the compressor. As revealed by Eq. (48), the input power of the compressor has a linear relation with the quantity of hydrogen compressed. Constraint (49) guarantees that the input power must be within its rated power.

3.3.2. Operation constraints of hydrogen tank

Constructing a network of pipelines for the real-time transportation of compressed hydrogen is not likely to be a practical option at present, due to the high initial investment cost associated with such scale of infrastructure. Instead, the gaseous high-pressure hydrogen can be transported to the hydrogen market at set times of the day by tube trailers—tube trailers are assumed to be provided by hydrogen wholesalers, so its CapEx and OpEx are hence ignored. From this viewpoint, a hydrogen tank is needed to store the hydrogen generated. The operation constraints of the tank, which share high similarities with those of battery storage, are:

$$\upsilon_H S_{\text{tank},\,t+1} = \upsilon_H S_{\text{tank},\,t} + \Delta t \left(D_{\text{elec},\,t} - D_{H,\,t} \right), \tag{50}$$

$$0 \le S_{\text{tank},\,t} \le \widetilde{S}_{\text{tank}}, \tag{51}$$

$$S_{\text{tank},\,1} = 0, \tag{52}$$

$$D_{H,\,t} = \begin{cases} S_{\text{tank},\,t}, & \text{if } t \bmod 24 = 0, \\ 0, & \text{otherwise}, \end{cases} \tag{53}$$

where $S_{\text{tank},\,1}$, $S_{\text{tank},\,t}$, and $S_{\text{tank},\,t+1}$ denote the respective volumes of hydrogen stored in the tank at time $t = 1$, t, and $t+1$; υ_H represents the mass volume fraction of hydrogen under the pressure of ϑ_{comp}; the symbol "mod" is the modulo operator. The hydrogen balance in the tank is realized by Eq. (50), which relates the volume of stored hydrogen to the hydrogen production rate of the electrolyzer and the volume of hydrogen for sale. Constraint (51) ensures that the volume of the stored hydrogen is restricted by its limiting value. The initial volume of hydrogen in the tank is set to be zero, as stated in Eq. (52). Constraint (53) assumes that wholesalers clear out the hydrogen from the tank at 12:00 midnight, resulting in a complete depletion of the stored hydrogen at that time. From Eq. (53), it also shows that the hydrogen demand is therefore not a constant but a variable, and is nonzero for only one hour of a day.

3.3.3. Operation constraints of PV plant

PV, which serves as the sole energy producer in the hybrid system, is able to take (a combination of) the following actions during any arbitrary hour: (1) sending power directly to fulfill the load demand, (2) charging the battery storage, (3) sending power to the hydrogen production system (powering both the electrolyzer and compressor), (4) being curtailed. (This can be also seen in Fig. 2, in which four arrows leave the PV plant.) Denoting the power corresponding to these five actions by $P_{\text{dir},\,t}$, $P_{\text{ch},\,t}$, $P_{\text{elec},\,t}$, $P_{\text{comp},\,t}$, and $P_{\text{cur},\,t}$, the power balance constraint writes:

$$P_{\text{dir},\,t} + P_{\text{ch},\,t} + P_{\text{elec},\,t} + P_{\text{comp},\,t} + P_{\text{cur},\,t} = X_s P_{\text{pv},\,t}, \tag{54}$$

where $P_{\text{pv},\,t}$ is the output power of the unconstrained PV plant at time t, and with the PV oversizing ratio X_s, the right-hand-side of Eq. (54) gives the overall PV power output. Besides the equality constraint, one has to be aware of the inequality bounding the overbuilding factor, that is,

$$1 \le X_s \le \overline{X}_s, \tag{55}$$

where $\overline{X}_s$ is the upper limit of the PV oversizing ratio. In practice, this upper limit may be set according to possible environmental restrictions such as a limited area for building the PV plant(s).

3.3.4. Power balance constraint

The load demand is to be jointly satisfied by PV and battery storage, which may be expressed mathematically as:

$$P_{\text{load},\,t} = P_{\text{dir},\,t} + P_{\text{dis},\,t}, \tag{56}$$

where $P_{\text{load},\,t}$ denotes the load demand at time t. Setting constraint (56) ensures that the PBH hybrid system can meet the load on a 24/365 basis without load shedding.

3.4. Model algorithm

To demonstrate the implications of using refined modeling for three main energy components in terms of capacity optimization and performance evaluation, two cases, denoted as Case A and Case B, are considered, which correspond to the generic modeling and the refined modeling introduced in Section 2.

- Case A: The core components, including PV, battery storage, and electrolyzer, are modeled with traditional/generic approaches. That is, the generic PV plant model A, the generic battery model A, and the generic electrolyzer model A are jointly considered in this case.

- Case B: The power output of PV is simulated using the model chain; the battery charging and discharging patterns are constrained by a measurement-based battery model; and the dynamic hydrogen production efficiency of the electrolyzer is incorporated into the operation modeling of the electrolyzer. In other words, the refined PV plant model B, the refined battery model B, and the refined electrolyzer model B are simultaneously adopted in this case.

On the one hand, the mathematical model under Case A is an MILP, for which an exact solution can be obtained through the well-established branch-and-bound method. The branch-and-bound method is implemented in most off-the-shelf solvers. Here, the Gurobi optimizer [55] as available on the Python-Spyder platform is used. On the other hand, the utilization of a piecewise linear function in Case B, which aims to represent the relation between the input power and hydrogen production rate of the electrolyzer, unavoidably introduces a complication during the optimization. More specifically, the rated power of the electrolyzer, as a variable within the optimization model, is positioned in the denominator, cf. Eq. (39), thereby resulting in a non-convex optimization model. As such, the aforementioned solver can no longer be adopted to attain the solution of the mathematical model under Case B.

However, upon scrutinizing the optimization model of Case B, one may notice that the model can be reduced to an MILP, if the number of battery storage and the rated power of the electrolyzer are fixed. In view of that, this work proposes using a hybrid algorithm that integrates a meta-heuristic technique such as PSO with the branch-and-bound method, for the purpose of obtaining a solution for Case B. The pseudo-code of the hybrid algorithm is presented in Algorithm 1. One should note that, insofar as meta-heuristic optimization is concerned, the exact solution cannot be guaranteed. Nevertheless, given the otherwise insoluble model, one ought to regard the meta-heuristic optimization as admissible. The focus here should rather be on the design of the meta-heuristic optimization, to ensure its maximum utility.

Algorithm 1 The proposed algorithm that combines particle swarm optimization and branch-and-bound method

Input: number of particles ($\overline{m}$), number of variables to solve ($\overline{d}$), maximum iteration number ($\overline{j}$), individual learning factor (c_1), social learning factor (c_2), maximum inertia weight ($\overline{w}$), minimum inertia weight ($\underline{w}$), $\overline{P}_{\text{elec}}$, $\overline{N}_b$, maximum particle velocity $\left(\overline{v}_d, d \in \{1, 2, \ldots, \overline{d}\}\right)$, and minimum particle velocity $\left(\underline{v}_d\right)$.
Output: N_b^* and P_{elec}^*

Initialize the velocity $\left(v_{m,d}^1, m \in \{1, 2, \ldots, \overline{m}\}\right)$ and position $\left(x_{m,d}^1\right)$ of each particle
for $j = 1, 2, \ldots, \overline{j}$ **do**
    Invoke the Gurobi solver to obtain the fitness value of each particle $\left(f_m^j\right)$
    Denote the individual optimum as $f_{m,\text{pbest}}$ and their corresponding positions as $p_{m,\text{pbest}}$
    if $f_m^j < f_{m,\text{pbest}}$ **then**
        $f_{m,\text{pbest}} \leftarrow f_m^j, \quad p_{m,\text{pbest}} \leftarrow x_m^j$
    end if
    Denote the population optimum as f_{gbest} and its corresponding position as p_{gbest}
    if $f_{m,\text{pbest}} < f_{\text{gbest}}$ **then**
        $f_{\text{gbest}} \leftarrow f_{m,\text{pbest}}, \quad p_{\text{gbest}} \leftarrow p_{m,\text{pbest}}$
    end if
    Update the velocity of each particle—r_1 and r_2 are random numbers generated following a uniform distribution between 0 and 1
    $v_{m,d}^{j+1} = w v_{m,d}^j + c_1 r_1 \left(p_{m,\text{pbest}} - x_{m,d}^j\right) + c_2 r_2 \left(p_{\text{gbest}} - x_{m,d}^j\right)$
    Update the position of each particle
    $x_{m,d}^{j+1} = x_{m,d}^j + v_{m,d}^{j+1}$
    Update the inertia weight of the algorithm
    $w = \overline{w} - \left(\overline{w} - \underline{w}\right) \times j/\overline{j}$
end for

The hybrid algorithm requires several input parameters, including the hyperparameters of the PSO (such as number of particles, number of variables to solve, or maximum iteration number), an upper limit value on the rated power of the electrolyzer $\left(\overline{P}_{\text{elec}}\right)$, and an upper limit value on the number of battery storage $\left(\overline{N}_b\right)$. Regarding the variables to solve, i.e., the output variables, there are two: the optimal number of battery storage $\left(N_b^*\right)$ and the optimal rated power of the electrolyzer $\left(P_{\text{elec}}^*\right)$. The algorithm typically begins with a randomly generated velocity and position for each particle, as shown in line 1—the position of each particle denotes a possible scenario for the values of $\widetilde{P}_{\text{elec}}$ and N_b. Subsequently, based on that particular position information, the Gurobi solver is invoked to get the objective function value of that particle. Stated differently, this step, see line 3, involves the operation of obtaining the fitness value of each particle. In particular, when the model is unsolvable under a given particle, the fitness value of that particle would be assigned with a sufficiently large value. Furthermore, lines 4–11 record the optimal fitness values for each particle and all particles, along with their respective positions, for the j^{th} iteration. Lines 12–17 update the velocity and position of each particle, as well as the inertia weight of the algorithm. The algorithm terminates once the number of iterations reaches a preset value. It should be mentioned that the hybrid algorithm only outputs the values of N_b^* and P_{elec}^*, whereas the optimal configuration of the PBH hybrid system and the operation strategy of each component can be acquired by calling the solver, with respect to the found N_b^* and P_{elec}^*.

4. Data and parameters

This section first introduces the two datasets used in the empirical part of the work, and, in the second part, the selection of model parameters is comprehensively documented, with the sources of parameters referenced.

4.1. Dataset description

Before the two datasets of concern are introduced, the concept of TMY, as to its making, ought to be first clarified. A TMY dataset encompasses hourly weather data over a full year, which is specifically constructed to represent the typical (i.e., median) conditions over multiple years. A TMY dataset is constructed on a month-by-month basis, and for each month, the one that best characterizes the median weather condition over multiple years is selected. For that reason, a TMY is usually composed of monthly data from different years. TMY can be used for modeling building load calculations and modeling renewable energy conversion system production. In this work, the first of the two datasets employed herein is simulated from the TMY that was generated using a combination of 1991–2005 NSRDB data and, if available, 1961–1990 NSRDB data for some specific locations [56], whereas the second one is created from 1998–2020 NSRDB data [57]. Obviously, the TMY would be different even for the same location when different multiyear data are used. Nevertheless, the potential impact of the time inconsistencies in the two datasets is expected to be small, due to the fact that TMY represents the typical conditions, which are stable if the period considered is long enough.

The first dataset used in this work is part of the Open Energy Information (OpEI) initiative, which is a community-driven data platform containing information relevant to a wide variety of energy-related topics. In particular, the dataset named "Commercial and Residential Hourly Load Profiles for all TMY3 Locations in the United States" [58], as released by the United States Department of Energy, is considered. This dataset contains load profiles for 936 locations, which are distributed fairly evenly over most of the United States. For each location, 16 sets of commercial load profiles and one set of residential load profiles are provided. In addition, the electric load, heating load, and cooling load with 8760 timestamps are all provided for each set of load profiles. In this work, the Winslow Municipal Airport (35.03° N, 110.72° W) in Arizona, United States, with a site number of 723740, is selected as the modeling location without loss of generality. More specifically, the load data consists of the electric load demand of 400 residential buildings with an hourly maximum of 2.73 MW. It should be noted that readers can select any other location of preference to replicate the experiment due to the generalizability of the present optimization model.

The second dataset used in this work is sourced from the NSRDB [30], which offers satellite-derived irradiance data across most of the Americas with a latitude range of −20° and 60° for more than 25 years. NSRDB is produced using the so-called "Physical Solar Model," which is a physical retrieval algorithm that leverages a rich collection of remote-sensing, geography, and reanalysis databases. Although the latest version of NSRDB has a temporal resolution of 5 min and a spatial resolution of 2 km, its temporal coverage is insufficient as this version of data is available only from 2019 onward [59]. Therefore, the preceding and arguably more stable version of NSRDB is herein used, which has a 30-min–4-km resolution. (To get the irradiance that corresponds to the "average" condition over an hour, the XX:30 time stamps are retained, and the XX:00 ones are removed.) NSRDB data can be accessed via the API, and the routine is available in both the Python `pvlib` package [60] and the R `SolarData` package [61]. The NSRDB TMY data that collocates with the aforementioned load location is downloaded.

4.2. Model parameters

On the basis of a comprehensive review of the literature and adequate market research, this subsection provides in order the values of the parameters as appeared in Sections 2.2–2.4 and 3.2–3.4, along with their sources. At this stage, one must note that the value range of a certain parameter may be quite large [62]. For instance, Glenk and Reichelstein [63] noted in their 2019 paper that the unit investment cost of the electrolyzer could vary between a minimum of 385 \$/kW and a maximum of 2068 \$/kW. The unstructured, heterogeneous, and autonomous nature of the parameter values typically results from differences in industrial-development level and economic policy across countries [64–66]. Accordingly, reasonable adjustment of parameter values is herein carried out to tailor the optimal configuration to the present situation.

For the PV plant itself, there are two distinct approaches for simulation. The first is to simulate the PV power output for any given rated power, and the other is to simulate the PV power output for a per unit plant and then use a multiplier to elevate the output in accord with the rated power. When the simulation needs to be conducted multiple times, e.g., with different load conditions, the second approach is preferred and thus used in this paper. A 1 MW PV plant is set as the per unit case. The basic design parameters of the per unit PV plant are listed in Table 1. The main components of the per unit PV plant comprise PV modules from Yingli Solar (model: YL 250P-29b) [67] and inverter from TMEIC (model: PVL-L0833GR) [68]. To calculate the output of the unconstrained PV plant, as stated in Section 2.2, TMY meteorological parameters, including wind speed, ambient temperature, surface albedo, BNI, DHI, and GHI, are obtained from NSRDB. The daily power outputs of the per unit PV plant, simulated with the generic PV plant model A and the refined PV plant model B, are respectively shown in Fig. 6(a) and (b) for visualization. The `pvlib-python` package is leveraged for the simulation of PV power. As can be seen from Fig. 6, the PV power generated from model B is slightly lower than that from model A. More specifically, the average daily PV power simulated from model B is 6.55% lower compared to that obtained from model A. This is attributed to the fact that the physical PV model chain enables a more realistic description of the irradiance-to-power conversion, thus resulting in more power loss with respect to overly optimistic generic PV modeling.

Table 1: Technical specifications of the per unit PV plant.

Parameters	Meanings	Values	Sources
p	SAPM model parameter	-3.56	[36]
$\widetilde{P}_{\mathrm{ac}}$	Rated output power of the inverter	833,000 W	[14]
q	SAPM model parameter	-0.075	[36]
S	Tilt angle of the PV array	35.03°	–
$T_{\mathrm{mod}}^{\mathrm{NOCT}}$	Nominal operating cell temperature of the PV module	46°C	[67]
γ_{mod}	Temperature coefficient of the PV module	-0.42 %/°C	[67]
$\eta_{\mathrm{inv}}^{\mathrm{norm}}$	Nominal efficiency of the inverter	98.5%	[68]
ΔT	SAPM model parameter	3°C	[36]

As outlined in Section 2.3, battery charging/discharging measurements are needed to accurately capture the operating characteristics of the battery storage. In this work, these measurements consist of 20 charging sample points and 14 discharging sample points, measured on a testing battery with a rated capacity ($S_{b,\mathrm{ref}}$) of 5.32 kWh [69]. The remaining technical parameters as demanded by the model in Section 2.3 can be found in Table 2.

Table 2: Some technical parameters of battery storage.

Parameters	Meanings	Values	Sources
$\overline{N}_b$	Maximum value allowed for N_b	60,000	–
$\widetilde{P}_{\mathrm{ch}}$	Upper limit value of the charging power	$0.25\times S_b$	[18]
$\widetilde{P}_{\mathrm{dis}}$	Upper limit value of the discharging power	$0.25\times S_b$	[18]
$S_{b,\mathrm{ref}}$	Rated capacity of the testing battery	5.32 kWh	[69]
$\eta_{\mathrm{ch}}^{\mathrm{ref}}$	Charging efficiency of battery storage	95%	[14]
$\eta_{\mathrm{dis}}^{\mathrm{ref}}$	Discharging efficiency of battery storage	95%	[14]
σ_b	Self-discharge rate	0.01%	[14]
Δt	Time interval	1 h	–

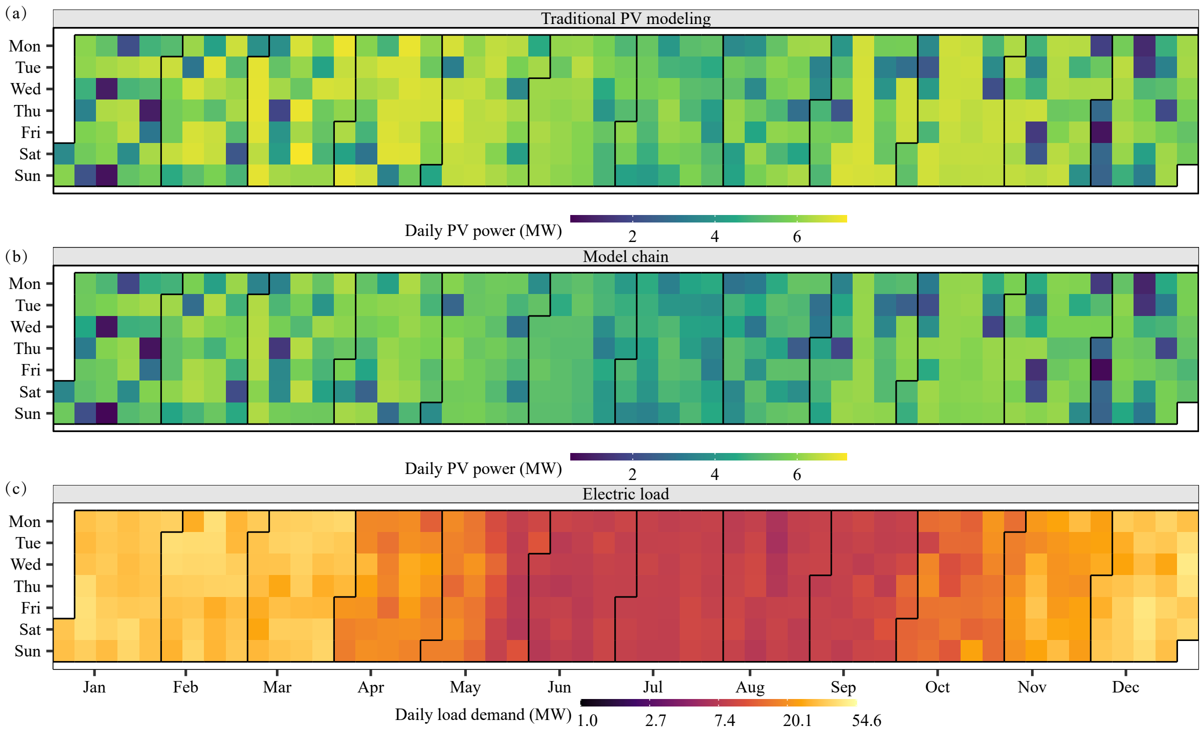

Fig. 6. The daily power output of the per unit PV plant, with a rated power of 1 megawatt, simulated by (a) generic PV modeling and (b) physical PV model chain. The plant is assumed to be situated at Winslow Municipal Airport (35.03° N, 110.72° W), in Arizona, United States. Subplot (c) represents the daily load demand of a residential building cluster situated around the same location, which should be fulfilled with 100% certainty.

Proton exchange membrane (PEM) electrolyzers, or simply electrolyzers hereafter, have the ability to accommodate fluctuations in PV power output, and are thus selected for the production of hydrogen using curtailed solar energy. The related technical parameters are summarised in Table 3. As depicted in Fig. 5 and described in Section 2.4, the rated power of the electrolyzer, as well as the number of line segments of the piecewise linear function, needs to be specified before using the refined electrolyzer model B. Moreover, the left endpoint, right endpoint, slope, and intercept of each line segment are determined by the differential evolution algorithm as available in the Python `pwlf` package [51]. In this work, the number of line segments is taken to be 5. As an illustration, Fig. 7 shows the hydrogen production efficiency, real hydrogen production rate, and fitted hydrogen production rate of a 200-kW electrolyzer with different power inputs. The figure evidently indicates that the piecewise linear function provides an excellent fit to the "input power–hydrogen production rate" curve of the electrolyzer.

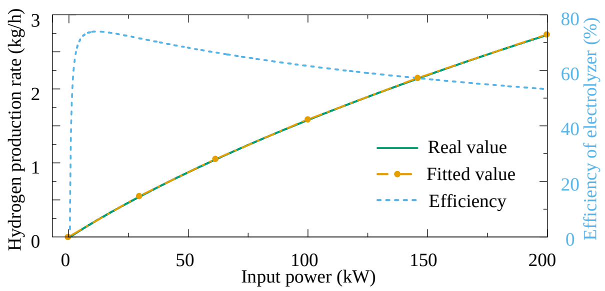

Fig. 7. Relationship between input power, hydrogen production efficiency, real hydrogen production rate, and linearly fitted hydrogen production rate for a 200-kW electrolyzer.

Table 3: Some technical parameters of the electrolyzer.

Parameters	Meanings	Values	Sources
D_H	Hydrogen diffusivity coefficient	4.9706×10^{-10} m^2/s	[20]
e_A	Anodic current collector thickness	1.4×10^{-3} m	[49]
e_C	Cathodic current collector thickness	2.35×10^{-4} m	[49]
e_M	Average membrane thicknes	9.04×10^{-5} m	[20]
F	Faraday constant	9.6485×10^4 C/mol	[50]
$\widetilde{i}$	Rated value of the current density	2×10^4 A/m^2	[20]
$i_{0\text{A}}$	Anodic exchange current density	4.1367×10^{-5} A/m^2	[20]
k	Average electrolyte conductivity	2.9693 S/m	[20]
ΔP	Pressure difference across the electrolyzer membrane	3×10^6 pa	[47]
R	Ideal gas constant	8.3144 J/(mol·K)	[50]
S_H	Hydrogen solubility coefficient	2.7807×10^5 mol/(pa·m^3)	[47]
T_0	Operating temperature	333 K	[46]
z	Stoichiometric coefficient	2	[49]
α_A	Charge transfer coefficient at the anodic side	0.65	[49]
γ_A	Anodic rugosity factor	150	[49]
σ_A	Conductivity of the anodic current collector	1.37×10^4 S/m	[49]
σ_C	Conductivity of the cathodic current collector	46 S/m	[49]

The load demand that needs to be satisfied by the PBH hybrid system on a 24/365 basis is displayed in Fig. 6(c). The load data is extracted from the OpEI dataset, as discussed in Section 4.1. Although the power output of the per unit PV plant has been acquired, one still has to design an unconstrained PV plant that can match/meet the load demand. The rated power $\left(\widetilde{P}_s\right)$ of the unconstrained PV plant can be estimated by the following equations [70]:

$$\widetilde{P}_s = \frac{\text{Daily load demand}}{\text{PGF} \times \Delta t}, \tag{57}$$

$$\text{PGF} = \frac{f_{\text{PV}} \times \text{Global daily horizontal irradiance}}{1000\,\text{W/m}^2}, \tag{58}$$

where PGF is the panel generation factor; f_{PV} is the PV derating factor, which is assumed to be 0.621 in this work [71]. According to Eqs. (57) and (58), the value of $\widetilde{P}_s$ is computed to be 5.93 MW.

Finally, the input parameters required by the optimization model, as discussed in Section 3.2–3.3, are provided in Table 4. As for the PSO–Gurobi hybrid algorithm, as elaborated in Section 3.4, its hyperparameters are detailed in Table 5. It is noted that most of the hyperparameters are set according to personal experience, since the optimization problem at hand is entirely new, and the existing parameter setting used in the literature has little advisory effect.

5. Result and discussion

Overall, Section 5.1 highlights the implications of the refined modeling for the system's main constituents on the cost of firm solar power delivery, especially in comparison to the generic model. Afterward, the influence of PV overbuilding and the hydrogen system on the firm kWh premium is investigated in Section 5.2. Further, Section 5.3 reveals the response of the firm kWh premium to different PV and battery costs. Lastly, Section 5.4 assesses the sensitivity of the main component ratings and firm kWh premium of the PBH hybrid system concerning variations in the electrolyzer cost.

5.1. Result comparison between generic and refined component modeling

The optimization models of Case A and Case B are solved using the algorithms outlined in Section 3.4, and the component sizes of the PBH hybrid system, as shown in Table 6, are obtained for both cases. The results show that all components have been configured in both cases, despite that the component sizes are quite different. For example, the rated power of the firm PV plant under Case A is 10.48 MW, whereas that of 12.12 MW under Case B represents a 16% increase. Additionally, the rated capacity of battery storage under Case B is 11% lower than that under Case A.

Undoubtedly, the disparity in component capacity has implications on the economics of the PBH hybrid system. Table 7 showcases the firm kWh premium and a detailed breakdown of the equivalent annual cost of generation under both cases. As seen from Table 7, the equivalent annual cost of the hydrogen system, the equivalent annual cost of PV, and the annual hydrogen sale revenue under Case B are about 47%, 16%, and 50% higher than those under Case A,

Table 4: Main input parameters of the optimization model.

Parameters	Meanings	Values	Sources
c_b	Unit investment cost of battery storage	137 \$/kWh	[10]
c_{comp}	Unit investment cost of compressor	730 \$/kW	[14]
c_{elec}	Unit investment cost of electrolyzer	1027.5 \$/kW	[43]
c_s	Unit investment cost of PV	833 \$/kW	[10]
c_{tank}	Unit investment cost of hydrogen tank	9292.5 \$/m^3	[14]
H_h	Hydrogen high heating value	39 kWh/kg	[14]
l_b	OpEx factor of battery storage	0.02%	[53]
l_{comp}	OpEx factor of compressor	1%	[14]
l_{elec}	OpEx factor of electrolyzer	5%	[14]
l_s	OpEx factor of PV	1%	[10]
l_{tank}	OpEx factor of hydrogen tank	1%	[14]
$p_{\text{comp}}^{\text{ref}}$	Standard hourly energy consumption of the compressor	2.1 kWh/(kg·h)	[52]
T_b	Lifetime of battery storage	15 yr.	[10]
T_{comp}	Lifetime of compressor	20 yr.	[14]
T_{elec}	Lifetime of electrolyzer	10 yr.	[43]
T_s	Lifetime of PV	30 yr.	[10]
T_{tank}	Lifetime of hydrogen tank	20 yr.	[14]
$\overline{X}_s$	Upper limit of the PV oversizing ratio	10	–
λ_H	Hydrogen sale price	5 \$/kg	[43]
υ_H	Mass volume fraction of hydrogen under the pressure of ϑ_{comp}	30 kg/m^3	[72]
$\eta_{\text{elec}}^{\text{ref}}$	Reference hydrogen production efficiency of the electrolyzer	67%	[73]
ϑ_0	Standard atmospheric pressure	1 bar	[52]
ϑ_{comp}	Normal working pressure of the compressor	200 bar	[52]
$\vartheta_{\text{comp}}^{\text{ref}}$	Standard working pressure of the compressor	350 bar	[52]
τ_0	Discount rate	8%	[18]

Table 5: Parameters of the particle swarm optimization–Gurobi hybrid algorithm designed to get the solution for Case B.

Parameters	Meanings	Values	Sources
c_1	Individual learning factor	1.5	[74]
c_2	Social learning factor	1.5	[74]
$\overline{d}$	Number of variables to solve	2	–
$\overline{j}$	Maximum iteration number	50	–
$\overline{m}$	Number of particles	20	–
$\overline{P}_{\text{elec}}$	Upper limit value on the rated power of the electrolyzer	$\widetilde{P}_s$	–
$\overline{v}_1$	Maximum particle velocity for $\widetilde{P}_{\text{elec}}$	$10\% \times \overline{P}_{\text{elec}}$	–
$\underline{v}_1$	Minimum particle velocity for $\widetilde{P}_{\text{elec}}$	$-10\% \times \overline{P}_{\text{elec}}$	–
$\overline{v}_2$	Maximum particle velocity forN_b	$10\% \times \overline{N}_b$	–
$\underline{v}_2$	Minimum particle velocity for N_b	$-10\% \times \overline{N}_b$	–
$\overline{w}$	Maximum inertia weight	0.8	[74]
$\underline{w}$	Minimum inertia weight	0.4	[74]

Table 6: Optimal component capacities of the PV–battery–hydrogen hybrid system under Case A and Case B. The error percentage is computed by dividing the difference in rated values between both cases by the rated value of Case A.

	Case A	Case B	Error percentage
Rated power of firm PV plant	10.48 MW	12.12 MW	15.65%
Rated capacity of battery storage	72.89 MWh	64.90 MWh	−10.96%
Rated power of electrolyzer	2.23 MW	3.27 MW	46.64%
Rated power of compressor	0.07 MW	0.12 MW	71.43%
Rated capacity of hydrogen tank	10.49 kg	20.86 kg	98.86%

respectively. The reason for this discrepancy can be attributed to the installation of a higher-capacity electrolyzer, a larger hydrogen tank, and a larger PV plant in Case B, as compared to Case A (cf. Table 6). However, given the deployment of battery storage with a smaller rated capacity under Case B, the equivalent annual cost of battery storage is 10% lower than that of Case A. On this point, the equivalent annual cost of generation for the PBH hybrid system can be calculated based on Eq. (46), and the firm kWh premium is computed using Eqs. (44)–(45). The equivalent annual cost of generation amounts to 1913×10^3 \$ under Case B, compared to 2019×10^3 \$ under Case A, indicating approximately a 5% reduction. Besides, the firm kWh premium under Case B exhibits an 11% decrease when compared to Case A.

As shown in Table 7, the use of generic component modeling for the main components overestimates the equivalent annual cost of generation or firm kWh premium for the PBH hybrid system. Considering that the difference between

Table 7: Comparison of the economics of the PV–battery–hydrogen hybrid system under Case A and Case B. The error percentage is computed by dividing the difference in economic values between both cases by the respective value of Case A.

	Case A	Case B	Error percentage
Equivalent annual cost of hydrogen system (10^3\$)	476.41	699.03	46.73%
Equivalent annual cost of PV (10^3\$)	862.58	997.64	15.66%
Equivalent annual cost of battery storage (10^3\$)	1332.65	1193.40	−10.45%
Annual hydrogen sale revenue (10^3\$)	652.29	977.52	49.86%
Equivalent annual cost of generation (10^3\$)	2019.35	1912.55	−5.29%
Firm kWh premium (dimensionless)	6.53	5.78	−11.49%

Case A and Case B only lies in the main component modeling, it can be concluded that the modeling of component operation in a more refined/realistic fashion is crucial for the economics of the PBH hybrid system. Particularly, this conclusion is provided at a holistic level because the modeling techniques for the three main components in the two cases differ. Stated differently, determining the influence of refined modeling for a single component on the firm kWh premium is challenging. To complement the comparative analysis of individual component-wise model replacement, Appendix A offers a detailed discussion. The general finding is that employing a generic model for any of the main components can lead to an overestimation of the firm kWh premium, albeit to varying degrees.

Notwithstanding, though this case study reveals a reduction in the cost of stabilized PV power generation when the refined component models are utilized, other cases might increase the cost, which depends on the parameter assumptions of the generic component models; the analysis has to be done on a case-by-case basis. Certainly, the above result aligns with existing research. For instance, Yang et al. [14] confirmed that the physical PV model chain can elevate the annual profit of a PV–hydrogen hybrid system in comparison to generic PV modeling. Mu et al. [75] indicated that incorporating the variable energy conversion efficiencies into the optimal configuration model, instead of relying on fixed efficiency assumptions, has the potential to shorten the payback period of the system. Similarly, Ma et al. [43] denoted that the overall profitability of the offshore wind–hydrogen–battery system is enhanced once the non-linear efficiencies of the battery storage and hydrogen plant are jointly considered in the co-optimization of the component sizing and energy management.

5.2. Benefits of PV overbuilding and hydrogen system installation

As mentioned in Section 5.1, the cost of firm PV generation can be accurately obtained by employing refined component modeling, that is, the granularity of modeling ought to be ensured as much as possible when developing an optimization for the lowest firm solar power delivery. Nevertheless, it should be noted that when applying the PSO–Gurobi hybrid algorithm proposed in Section 3.4 to solve the non-convex mathematical model embedded with refined component modeling, the execution time of the algorithm program can be as long as 6 hours, in comparison to the 1-minute run time of using generic modeling. Besides, the results might be trapped in a local optimum owing to the involvement of PSO. Bearing this in mind, the analysis conducted in the following subsections relies on the solution process of Case A, as discussed in Section 3.4.

This subsection first outlines the superiority of PV overbuilding in reducing the firm kWh premium, followed by the advantages of installing a hydrogen system in a PV–battery hybrid system. In a previous study by Yang et al. [14], a PV–battery hybrid system built to meet a yearly constant load was analyzed to reveal the effect of different PV oversizing ratios (X_s) on the firm kWh premium. That study was performed by fixing a range of X_s values and subsequently optimizing the installed capacity of battery storage together with the resultant firm kWh premium for each X_s value. Similarly, the X_s values in this paper are drawn from the set of $\{1, 1.01, \cdots, 8\}$ in steps of 0.01, and the PV–battery hybrid system is built to meet the actual load profile. The firm kWh premiums at these X_s values are illustrated in Fig. 8(a). Consistent with the findings in [14], Fig. 8(a) shows that the firm kWh premium reaches its peak value when the PV-firming strategy contains battery storage alone, see point A; the firm kWh premium drops rapidly to its lowest point (point B) when the overbuilt PV and battery storage are placed with optimized capacities; as the value of X_s rises further, the firm kWh premium represents a quasi-linear growth trend. As for Fig. 8(c), it shows the variations in the contributions for PV and battery costs to the firm kWh premium in relation to the PV oversizing ratios ranging from 1.3 to 6. More specifically, the PV cost contribution increases but the battery cost contribution declines when the PV oversizing ratio goes up. These results imply that it is vital to enlarge the installed capacity of the PV plant owing to the high cost of firm PV power achieved by a battery-only solution. The explanation for this

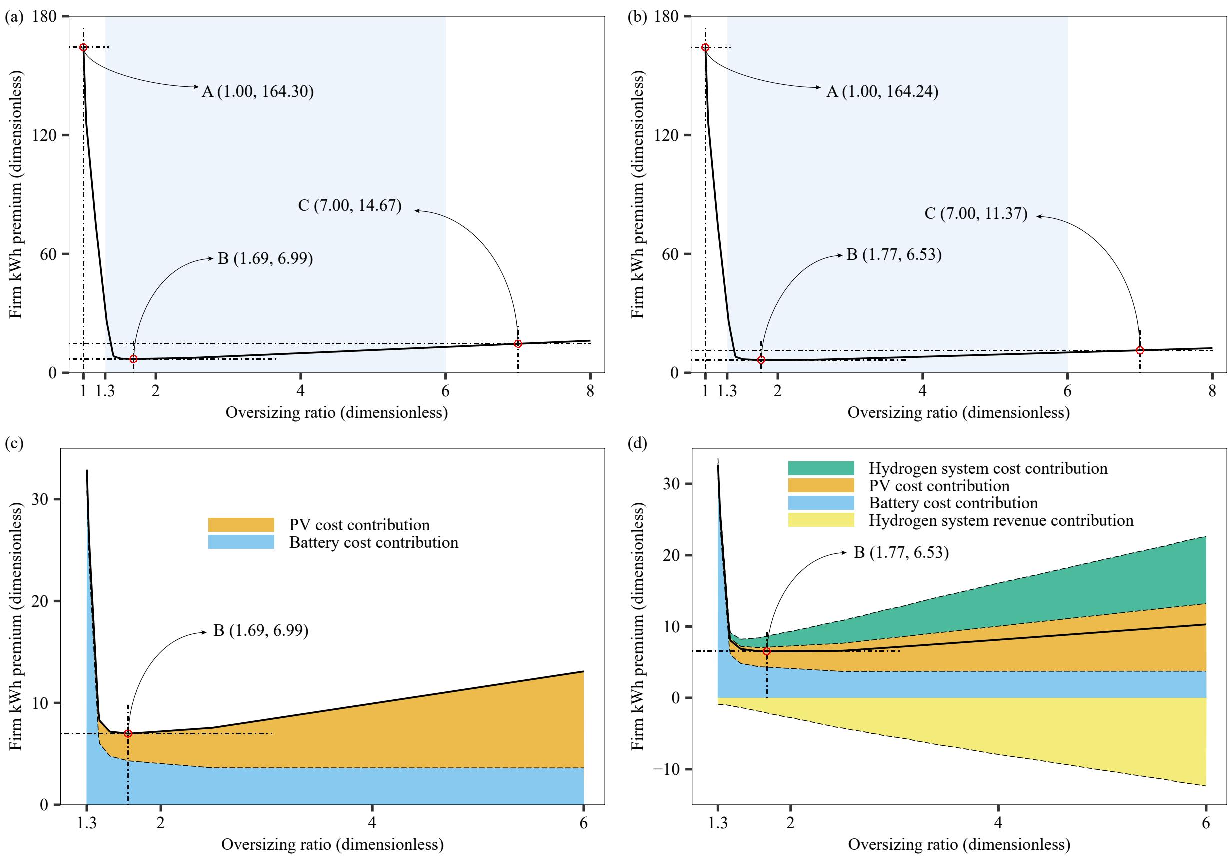

Fig. 8. Firm kWh premiums versus the PV oversizing ratios spanning from 1 to 8 with an interval step of 0.01 for a PV–battery hybrid system (a) without and (b) with a hydrogen system. Points A and C in each subplot represent scenarios where the PV oversizing ratio is set to be 1 and 7, respectively, whereas point B denotes the scenario where the optimal firm kWh premium is achieved. Subplots (c) and (d) correspond to the light blue areas of subplots (a) and (b), and present a breakdown of the firm kWh premium.

phenomenon is as follows: Before X_s exceeds the minimum value (point B), the cost saved by reducing excess battery storage is adequate to offset the additional cost incurred by PV overbuilding. More details can be found in [14].

In general, the practice of PV overbuilding is accompanied by an elevation in the PV curtailment rate. For example, the PV curtailment rates at points A, B, and C in Fig. 8(a) are 20%, 60%, and 90%, respectively.[1] It is evident that PV overbuilding conflicts with the conventional principle of mitigating PV curtailment. Considering the nearly negligible cost of curtailed solar power, the intermittent and free curtailed electricity can be effectively utilized to electrolyze water and generate hydrogen for commercial purposes, thereby further cutting down the firm kWh premium of the PBH hybrid system—recall that this is one of the innovations in this work. The firm kWh premiums of the PV–battery hybrid system equipped with a hydrogen system, as well as the composition of the firm kWh premium over a range of X_s values, are depicted in Fig. 8(b) and (d).

From these two subplots, one can observe that the pattern of change in the costs of the PV plant and battery storage with respect to the PV oversizing ratio in the PBH hybrid system is the same as in the PV–battery hybrid system. The costs associated with the hydrogen system, as well as the revenues generated from hydrogen sales, both rise as X_s increases. However, it is evident that the revenues from hydrogen sales consistently surpass the costs of the hydrogen

[1]It is noteworthy that the term "oversizing ratio" in this work is different from that introduced by Perez et al. [6]. The former pertains to the multiplier applied to the unconstrained PV capacity, whereas the latter refers to the inverse of the curtailed PV fraction. Stated differently, even if there is no overbuilding in this work, i.e., $X_s = 1$, the optimization can still curtail some power from the unconstrained PV plant, resulting in a non-zero value of the PV curtailment rate at point A in Fig. 8(a).

system at all X_s values. On this account, installing a hydrogen system in the PV–battery hybrid system always lowers the cost of a firm solar kWh. As shown in Fig. 8, the optimal firm kWh premium of a PV–battery hybrid system is 6.99, whereas the minimum firm kWh premium of the PBH hybrid system is 6.53, indicating that the installation of a hydrogen system reduces the firm kWh premium by up to 6.58%. Moreover, the deployment of a hydrogen system also contributes to the decrease in the PV curtailment rate. This can be seen from the PV curtailment rates at points A, B, and C in Fig. 8(b), which are recorded as 0%, 24%, and 26%, respectively. It is noteworthy to highlight that the utilization of curtailed renewable energy has been receiving growing attention in academia. Alkhalidi et al. [76] exploited the curtailed wind energy in Jordan to charge local electric vehicles, demonstrating that this strategy can turn the wind energy oversupply into profit and mitigate the wastage of resources. Park et al. [77] put forward an optimization model to determine the optimal sizes of hydrogen plants and assess the economic viability of hydrogen production through the utilization of curtailed wind and solar energy.

5.3. Effect of PV and battery costs on the firm kWh premium

As demonstrated in Fig. 2, the concurrent installation of both a PV plant and battery storage is crucial within a PBH hybrid system. This is because the PV plant serves as the sole energy producer, while the battery storage plays a pivotal role in guaranteeing the firm power supply 100% of the time, particularly during periods of low or zero PV power availability, such as rainy days or nighttime. According to the optimization results under Case-B, as listed in Table 7, the equivalent annual costs of the PV plant and battery storage, which are largely dominated by their respective unit investment costs, accounting for 64% and 59% of the equivalent annual cost of generation, respectively—the sum of the two exceeds 100% due to the profit from the hydrogen production system. This suggests that the unit investment costs of the PV plant and battery storage have a notable impact on the firm kWh premium of the PBH hybrid system. To that end, a sensitivity analysis of the firm kWh premium relative to unit PV and battery costs is performed in this subsection. To be more specific, the unit investment cost of the PV plant (c_s) is taken from the set of $\{300, 320, \cdots, 1000\}$ with an interval step of 20 \$/kW, whereas the unit investment cost of battery storage (c_b) is selected from the set of $\{30, 40, \cdots, 180\}$ with an interval step of 10 \$/kWh. This assumption guarantees that "all" future PV and battery cost combinations can be covered to the greatest extent possible. Furthermore, the decision not to decrease c_s below 300 \$/kW is to avoid a scenario where it becomes financially feasible to establish a PV plant solely for hydrogen production, disregarding other energy generation objectives. In such a scenario, the PV plant would be constructed with an oversizing ratio that reaches the predefined limit, which falls outside the scope of this study and is not a reasonable assumption considering the existing state of hydrogen production technology [78]. Fig. 9 depicts the contour plots of the main component ratings and economics of the PBH hybrid system across different combinations of unit PV and battery costs.

As shown in Fig. 9(a) and (b), the rated capacity of battery storage and the rated power of the PV plant exhibit a strong correlation with the unit PV and battery costs. Specifically, when the value of c_s increases relative to the value of c_b, the hybrid system tends to configure battery storage with a larger rated capacity. Conversely, when the value of c_s decreases in comparison to c_b, increasing the PV oversizing ratio becomes the preferred option. It is worth noting that there are large areas of identical color in Fig. 9(a) and (b), which can be explained as follows: The objective of building a PBH hybrid system is to fulfill the 24/365 load demand at all times with 100% certainty at the lowest cost, which indicates that battery storage and PV plant with adequate capacities should be installed as a first priority to maintain power balance within the system, that is, variations in unit PV and battery costs may not work in certain cases. Since the electrolyzer is leveraged for hydrogen production through curtailed solar energy, its rated power is approximately proportional to the rated power of the PV plant, as depicted in Fig. 9(b) and (c). On the other hand, Fig. 9(d) displays that a decrease in either c_s or c_b reduces the equivalent annual cost of generation of the hybrid system. As specified by Eq. (45), the LCOE of firm PV is defined as the ratio of the equivalent annual cost of generation to the annual load demand. Given the fixed load demand, the LCOE of firm PV follows a similar pattern of variation as the equivalent annual cost of generation, as illustrated in Fig. 9(d) and (f). Nevertheless, the firm kWh premium reaches its lowest value when the unit PV cost is highest and the unit battery cost is lowest, see the bottom-right corner of Fig. 9(e). This is governed by the concept of firm kWh premium: When the PV cost is more expensive compared to the battery cost, the cost of firm solar power relative to unconstrained PV power decreases.

Currently, in certain countries like China, unconstrained PV power has been declared to have achieved grid parity [81], yet this is not entirely true, as the power grid needs additional costs to deploy excess backup to eliminate the volatility of unconstrained PV. For instance, in the case of the PBH hybrid system analyzed in this study, the optimal

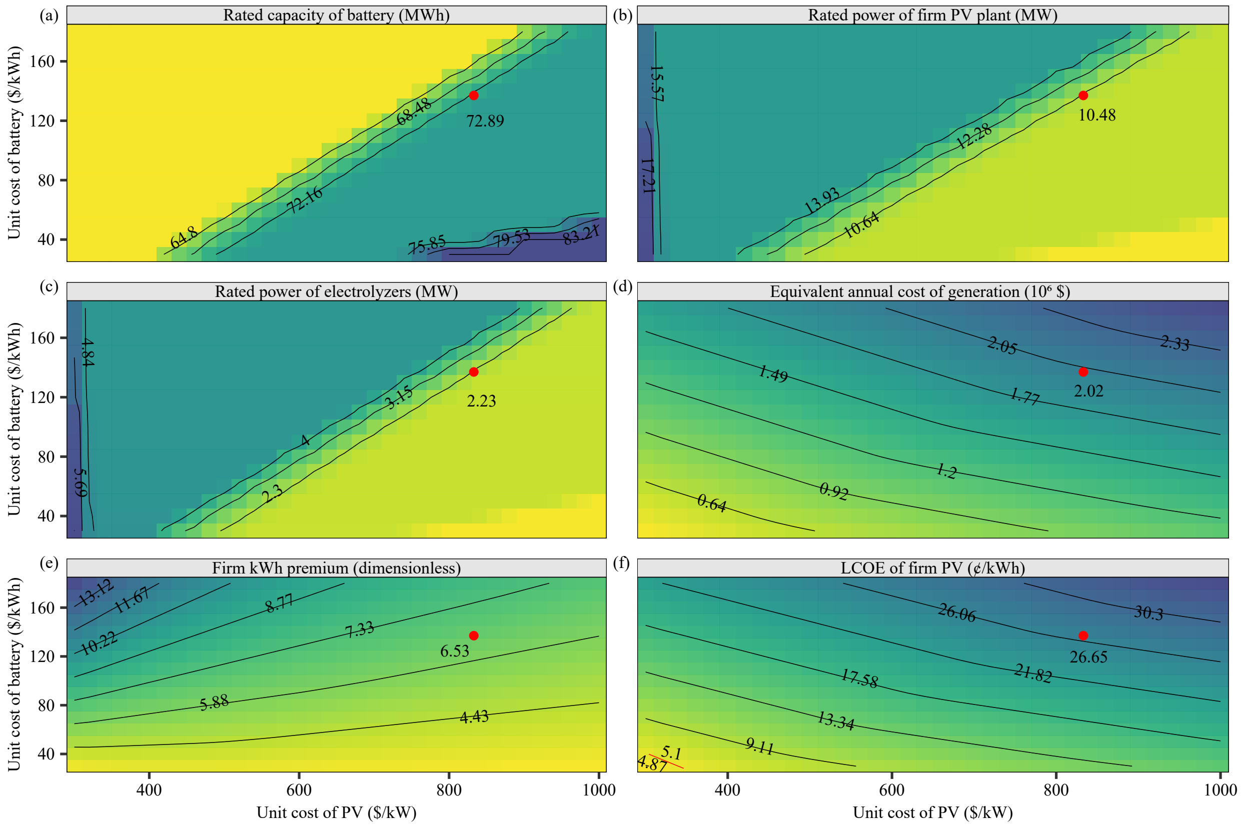

Fig. 9. The rated capacity of battery storage (a), rated power of firm PV plant (b), rated power of electrolyzer (c), equivalent annual cost of generation (d), firm kWh premium (e), and levelized cost of electricity of firm PV (f) for the PV–battery–hydrogen hybrid system across different combinations of unit PV and battery costs. The red dot within each subplot signifies the scenario where the unit PV cost is 883 \$/kW and the unit battery cost is 137 \$/kWh, which corresponds to Case A as described in Section 5.1. In addition, the red line in the bottom-left corner of subplot (f) indicates the current average feed-in tariff in China [79, 80].

firm kWh premium under Case A is 26.65 ¢/kWh, which is 5.23 times higher than the current average feed-in tariff in China (5.10 ¢/kWh) [79, 80]. As shown in Fig. 9(f), to achieve true grid parity of PV, the values of c_b (unit battery cost) and c_s (unit PV cost) should be below 30 \$/kWh and 300 \$/kW, respectively. Measures employed to reduce unit PV and battery costs encompass technological innovation and policy incentives. These values are in line with those calculated in the study by Yang et al. [14], who denoted that when the unit costs of battery and PV decline to 40 \$/kWh and 250 \$/kW, the LCOE of firm PV employed to supply a flat base load could drop below 5.10 ¢/kWh.

5.4. Sensitivity to electrolyzer cost

In the preceding analysis, the unit investment cost (c_{elec}) of the electrolyzer, a critical component in the PBH hybrid system, is treated as a fixed parameter. Nonetheless, as highlighted by Glenk and Reichelstein [63], the c_{elec} value differs considerably from one country to another due to varying economic development and government support. Besides, with the advancement of technology and the maturation of the market, the c_{elec} value is expected to be further reduced in future. From this perspective, this subsection perturbs the value of c_{elec}, so as to investigate the potential of a hydrogen system in reducing the cost of delivering firm solar generation. Similar to the reason that the value of c_s in Section 5.3 is not less than 300 \$/kW, the c_{elec} values are chosen from the set of $\{550, 560, \cdots, 1100\}$ with a step size of 10 \$/kW. The main component ratings and firm kWh premium under different unit electrolyzer costs are presented in Fig. 10.

As illustrated in Fig. 10(a), the configured rated power of the electrolyzer increases with decreasing c_{elec}. This phenomenon can be attributed to the relationship between electrolyzer cost reduction and increased profitability from

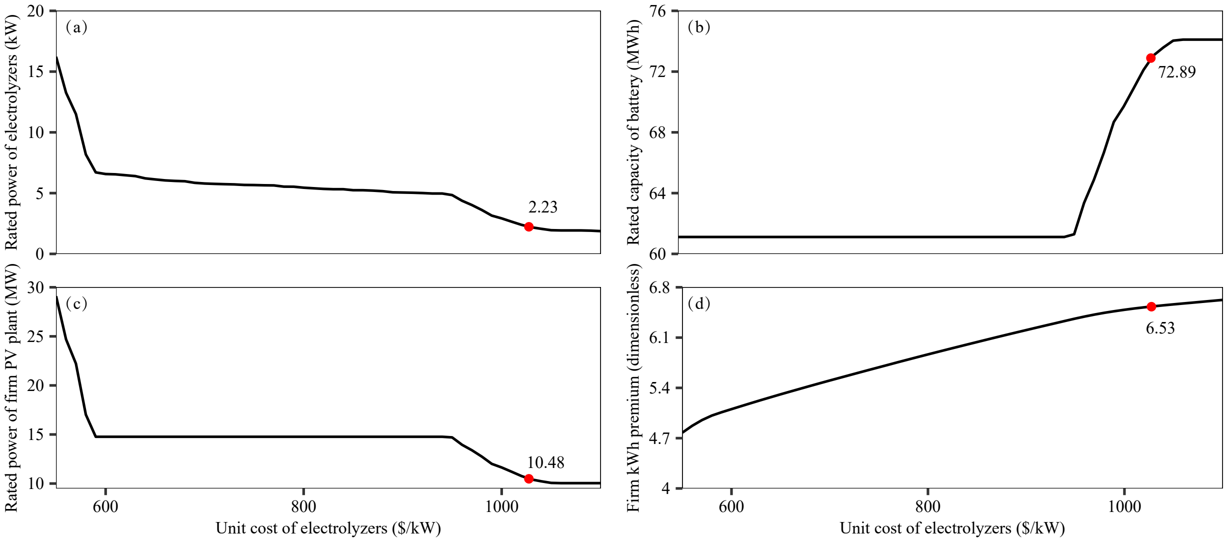

Fig. 10. The rated power of electrolyzer (a), rated capacity of battery storage (b), rated power of firm PV plant (c), and firm kWh premium (d) of the PV–battery–hydrogen hybrid system as a function of the unit electrolyzer cost. The red dot within each subplot shows the optimization results under the current electrolyzer cost, that is, c_{elec} = 1027.5 $/kW, see Case A in Section 5.1 for more details.

hydrogen sales, leading to the preference for higher-capacity electrolyzers. With no surprise, a decrease in c_{elec} correlates with an increase in the rated power of the PV plant, see Fig. 10(c). This variation can be explained by the ability of the PV plant to generate a greater amount of electricity, enabling higher hydrogen production in response to the reduced electrolyzer cost. A similar trend can be observed in the power ratings of the electrolyzer and PV plant, as depicted in Fig. 10(a) and (c). This trend demonstrates an approximate correspondence between the two variables, as also evident in Fig. 9(b) and (c). With an increase in the rated power of the PV plant, the duration of direct supply from the PV plant itself extends, leading to a decrease in the required rated capacity of battery storage. Therefore, Fig. 10(b) demonstrates a pattern where the rated capacity of battery storage decreases as the value of c_{elec} declines. However, similar to the observations in Fig. 9(a) and (b), a range can be identified in both Fig. 10(b) and (c) where the ratings of the components are not significantly influenced by the value of c_{elec}. As for the firm kWh premium of the PBH hybrid system, it gradually decreases with decreasing c_{elec}, which can be seen in Fig. 10(d). More specifically, the firm kWh premium drops from 6.62 to 4.78 when the value of c_{elec} decreases from 1100 $/kW to 550 $/kW, which demonstrates the great potential of a hydrogen system to lower the cost of achieving firm PV generation.

In contrast to the generic electrolyzer model that assumes a fixed hydrogen production efficiency, this study introduces a refined electrolyzer model that incorporates dynamic hydrogen production efficiency (see Section 2.4), accounting for variations in input power. As illustrated in Fig. 7, when the refined electrolyzer model is employed, the hydrogen production efficiency peaks in the low input power range, whereas the hydrogen production rate reaches its zenith at the rated power. Thus, it is necessary to analyze how the electrolyzer could strike a balance between minimizing electricity consumption and maximizing hydrogen production. Furthermore, what the impact of changes in c_{elec} would bring should also be explored under this circumstance. Note that the Case-B model is again used herein and is solved by the PSO–branch-and-bound hybrid algorithm. Figure 11 provides the distribution of input power (greater than zero) for the electrolyzer with different values of c_{elec}. It shows that the electrolyzer tends to operate close to its rated power, irrespective of its rated power value. This behavior is driven by the objective of maximizing hydrogen production. Nevertheless, when the value of c_{elec} drops, which means that the rated power increases—a one-to-one mapping can be found between the unit electrolyzer cost and its power rating in Fig. 10(a)—the number of operating points located in the low input power range rises, so as to reduce electricity consumption. Consequently, a reduction in the value of c_{elec} increases the probability of partial load operation for the electrolyzer, thereby promoting energy savings. Undoubtedly, as the value of c_{elec} is expected to continue declining in the future, the advantages of integrating a hydrogen system into the PV–battery hybrid system for energy conservation and consumption reduction will become increasingly apparent.

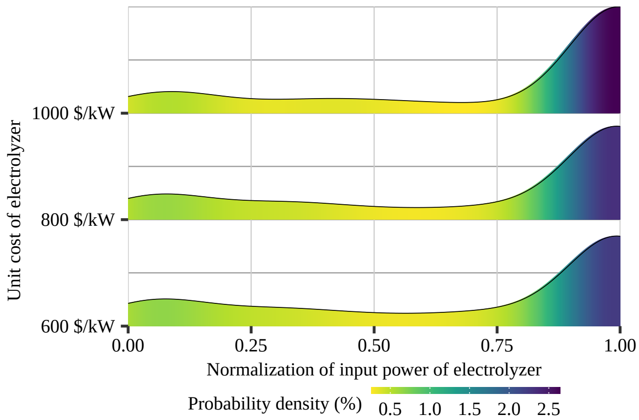

Fig. 11. The distribution of the input power (greater than zero) of the electrolyzer throughout all 8760 hours of a year with optimization conducted under different unit electrolyzer costs. The density function of each distribution is estimated using the `density` function in the `stats-R` package. The Gaussian function with a bandwidth of 0.1 is selected as the kernel function.

6. Conclusion

The concept of *firm generation* was proposed by Perez et al. [6] in 2019 to tackle the grid impacts due to the variability and intermittency associated with the unconstrained PV. The aim of firm generation is to completely eliminate discrepancies between solar generation and load demand by optimizing a mix of different firm power enablers, mainly including battery storage, geographical smoothing, demand response, and most importantly overbuilding & proactive curtailment. The measure that guides the optimization is known as the *firm kWh premium*. This measure, as defined in Eq. (44), quantifies the overall cost-effectiveness of firm PV power. On top of the firm generation concept, this work introduces a hydrogen system that consists of an electrolyzer, a compressor, and a hydrogen tank. The purpose of this system is to utilize the curtailed PV power, which is neither stored in the battery storage nor directly supplied to the load, for hydrogen production. This approach is motivated by the near-zero cost associated with the curtailed PV power. By incorporating the hydrogen system into the PV–battery hybrid system, a new revenue stream is revealed, which can further reduce the firm kWh premium. Besides the newly included hydrogen system, the effects of modeling granularity (i.e., generic versus refined) on the cost of firming up PV power are elucidated.

Using the PV–battery–hydrogen (PBH) hybrid system virtually situated at a mid-latitude site in the United States as a case study, it is observed that the level of modeling granularity for the main constituents significantly affects the ratings of the configured system equipment as well as the economics of the system. For instance, the difference in the rated power of firm PV plant between the two versions of modeling reaches 16%, while refined component modeling reduces the firm kWh premium by up to 11%, as compared to that of generic component modeling. This can be attributed to the inclusion of more detailed information in the refined main component modeling, resulting in optimized component sizes that better align with actual conditions. On this account, this work advocates the abandonment of simplified modeling of energy components, whenever possible, during the planning stage of the PBH hybrid system. Instead, it is preferable to employ refined component modeling that accurately captures the dynamic operating efficiencies.

Furthermore, the optimization results under Case A indicate that integrating a hydrogen system into the PV–battery hybrid system not only lowers the PV curtailment rate but also reduces the firm kWh premium. In the absence of a hydrogen system installation, the PV curtailment rate is 60% and the associated firm kWh premium is 6.99 at the optimal PV oversizing ratio; with the inclusion of a hydrogen system, the PV curtailment rate is reduced to 24%, accompanied by a firm kWh premium of 6.53. This observation can be attributed to the usage of the hydrogen system, which effectively consumes the surplus PV energy that would otherwise be curtailed and left unused by the load.

When the generic component modeling is adopted, the sensitivity analysis of various parameters yields the following findings : (1) With increasing PV oversizing ratio, the firm kWh premium decreases rapidly until reaching a minimum point, after which it rises quasi-linearly. (2) The firm kWh premium tends to decrease as the unit PV cost becomes greater relative to the unit battery cost. Nevertheless, a reduction in either unit PV cost or unit battery cost leads to a decrease in the LCOE of firm PV. Specifically, under the current parameter settings, the true grid parity of PV is attained when the unit PV cost is below 300 $/kW and the unit battery cost is below 30 $/kWh. (3) The firm kWh premium is closely related to the unit electrolyzer cost. As an example, once the unit electrolyzer cost is reduced by half, from 1100 $/kW to 550 $/kW, the firm kWh premium can be reduced by 28%. As shown in Fig. 11, the unit electrolyzer cost also affects the distribution of the electrolyzer input power. Precisely, a decrease in the unit electrolyzer cost leads to a rise in the rated power of the electrolyzer configured in the PBH hybrid system, see Fig. 10(a). In such a scenario, the decreased unit electrolyzer cost extends the duration in which the electrolyzer operates in the low input power range while maintaining high hydrogen production efficiency.

In the next phase, at least two directions can be considered for further investigation. Given that hydrogen will likely still be used for certain extant chemical syntheses in the future but its use for conventional fuel refining will likely end in tandem with the sunset of the fossil fuel era [82], the first is to replace hydrogen production with other electricity-consuming applications, such as irrigation, e-fuel production, or pumped hydro, as to explore whether the curtailed electricity of the PBH system could serve other purposes with quantifiable economic benefits. In other words, it would be great to add other electricity-consuming pathways into the current modeling architecture. This avenue is thought straightforward, so long as the models for those electricity-consuming applications are available. The second is to consider a cluster of PBH systems in a power system setting, where the areal load is jointly satisfied by those PBH systems. Compared to balancing power supply and demand in each region independently, energy sharing among the PBH-system cluster—the power deficit in one subarea is fulfilled by leveraging the PV output and battery discharging power from another subarea through connection transmission lines—can reduce both capital and operational expenditure. Therefore, determining the optimal component sizes for each PBH hybrid system and implementing power distribution and cost/revenue settlement between different systems deserves an in-depth analysis.

Appendix A. Comparative analysis: Substituting a generic model with component-by-component refined one

In Section 5.1, a result comparison is carried out, which contrasts the scenario where all system components are simulated using generic models (Case A) with that in which the main constituents, such as the PV, battery or electrolyzer, are all simulated using refined models (Case B). This comparison facilitates a comprehensive evaluation of whether adopting generic device models overestimates or underestimates the firm kWh premium of the PBH hybrid system, but what is the impact resulting from the utilization of a single generic component model remains undisclosed. From this point, this appendix endeavors to investigate the substitution of a generic model with a refined one on a component-by-component basis with the possibility of analyzing the effluence of each simplification. More specifically, three additional cases, denoted as Case C, Case D, and Case E, are introduced. Case C refers to the optimization model based on refined PV model B, generic battery model A, and generic electrolyzer model A. Case D refers to the optimization model based on generic PV model A, refined battery model B, and generic electrolyzer model A. Case E refers to the optimization model based on generic PV model A, generic battery model A, and refined electrolyzer model B. It can be observed that all three cases need to alter the modeling technique for a specific component compared to Case A.

Similar to Case A, the optimization model in Case C is an MILP, and the optimal solution can be directly obtained by invoking the Gurobi solver. Since there exist the bilinear terms in Eqs. (19)–(20), (23)–(24) and (26), the optimization problem of Case D is a bilinear programming. Here, the bisection-LP hybrid algorithm proposed by Yang et al. [10] is utilized to solve this model. As for Case E, its mathematical model is non-convex due to the presence of a variable situated in the denominator, cf. Eq. (39). Therefore, the PSO–Gurobi hybrid algorithm delineated in Section 3.4 is employed to get one acceptable solution. The optimal ratings of the components and economics of the PBH hybrid system under Cases A and C–E are shown in Table A.8.

It is evident from Table A.8 that the rated power of the firm PV plant in Case C is 7% lower than that in Case A. This is due to the fact that refined PV modeling simulates PV power in a more realistic fashion, as opposed to conventional PV modeling, which leads to a low power output, see Fig. 6. That said, the PV plant exhibiting a lower annual energy yield would be configured with a reduced rated value owing to its lower price-to-value ratio. Furthermore, when the power rating of PV decreases, the rated capacity of battery storage increases, but the nameplate value of each component in the hydrogen system declines. The former is attributed to the necessity of the PBH hybrid system to

Table A.8: Optimal configuration and economics of the PV–battery–hydrogen hybrid system under Cases A and C–E.

	Case A	Case C	Case D	Case E
Rated power of firm PV plant	10.48 MW	9.73 MW	10.11 MW	14.77 MW
Rated capacity of battery storage	72.89 MWh	76.41 MWh	68.79 MWh	61.11 MWh
Rated power of electrolyzer	2.23 MW	1.57 MW	2.26 MW	4.88 MW
Rated power of compressor	0.07 MW	0.05 MW	0.07 MW	0.17 MW
Rated capacity of hydrogen tank	10.49 kg	9.94 kg	14.63 kg	31.91 kg
Equivalent annual cost of hydrogen system (10^3\$)	476.41	334.57	483.90	1044.40
Equivalent annual cost of PV (10^3\$)	862.58	801.37	832.62	1215.71
Equivalent annual cost of battery storage (10^3\$)	1332.65	1389.30	1252.43	1148.20
Annual hydrogen sale revenue (10^3\$)	652.29	451.50	661.89	1472.68
Equivalent annual cost of generation (10^3\$)	2019.35	2073.73	1907.06	1935.62
Firm kWh premium (dimensionless)	6.53	6.27	6.17	6.26

firmly meet the load demand, whereas the latter is a consequence of the reduced curtailed PV output. There is no doubt that variations in equipment specifications influence the economics of the PBH hybrid system. The equivalent annual cost of generation in Case C is 2073.73 $\times 10^3$ \$, which is 3% higher than that in Case A. Nevertheless, the firm kWh premium of Case C is 4% lower than that of Case A. Note that when the premiums of Case A and Case C are computed using Eqs. (44)–(45), two of the four component involved in the premium calculation differ, including the equivalent annual cost of generation and the annual energy yield of unconstrained PV.

Table A.8 additionally illustrates that the use of a refined battery model (Case D) results in a reduction of the rated values for both PV plant and battery storage. The reason for this is that the measurement-based battery model allows the battery to operate with charging and discharging efficiencies close to unity, which can mitigate energy wastage and consequently reduce the requisite device capacity—further details can be seen in [10]. On the other hand, there exists a minimal disparity between the optimal component capacities of the hydrogen system in Case A and Case D. Overall, when the refined battery model is employed instead of the generic battery model, the equivalent annual cost of generation and firm kWh premium can be decreased by both 6%.

According to Table A.8, the rated power of the electrolyzer under Case E is nearly 2.5 times that of Case A. This could be explained by the tendency of the refined electrolyzer model to opt for a larger-capacity electrolyzer, which can fully exploit its high efficiency within the low input power range, see Fig.7. To align with the intentionally augmented rated power of the electrolyzer, the ratings of the PV plant, compressor, and hydrogen tank are correspondingly elevated. At this stage, the rated capacity of battery storage can be diminished owing to the notable advantage of PV overbuilding in reducing the cost of firm solar power delivery, as discussed in Section 5.2. Regarding the economics of the PBH hybrid system, which is predominantly influenced by the component ratings, one can observe that the equivalent annual cost of generation and firm kWh premium of Case E are both 4% lower than those of Case A.

In summary, the degree of modeling granularity applied to the PV, battery, and electrolyzer holds implications for the optimal component ratings and economics of the PBH hybrid system, thereby changing the value of the firm kWh premium. As shown in Table A.8, the premium for converting a variable solar kWh into a firm one is overestimated when relying solely on the generic model, be it for each of the main components. Precisely, the battery has the most substantial impact, followed by the electrolyzer, and the PV demonstrates the least influence. Moreover, when all three main components are modeled in a refined way, as in Case B, the firm kWh premium experiences the most significant decrease, which can be evidenced in Table 7. Accordingly, when the configuration of the PBH hybrid system is optimized, selecting refined component models emerges as the preferred choice in all circumstances.

Author Contributions

Guoming Yang: Conceptualization, Methodology, Software, Visualization, Writing – original draft. Dazhi Yang: Conceptualization, Formal Analysis, Resources, Funding Acquisition, Supervision, Writing – review & editing. Marc J. Perez: Investigation, Validation. Richard Perez: Formal analysis, Visualization, Validation. Jan Kleissl: Investigation. Jan Remund: Formal analysis, Visualization. Marco Pierro: Formal analysis, Visualization. Yuan Cheng: Validation. Yi Wang: Validation. Xiang'ao Xia: Investigation, Validation. Jianing Xu: Validation. Chao Lyu: Validation, Writing – review & editing. Bai Liu: Investigation, Validation. Hao Zhang: Validation, Resources, Supervision, Data curation, Writing – review & editing.

Conflicts of interest

There are no conflicts to declare.

Acknowledgments

Dazhi Yang and Hao Zhang are supported by the National Natural Science Foundation of China (project no. 42375192).

Dazhi Yang and Xiang'ao Xia are supported by the China Meteorological Administration Climate Change Special Program (CMA-CCSP; project no. QBZ202315).

Yuan Cheng and Yi Wang are supported by the Project of HIT–Hong Kong Exchanges.

Hao Zhang is supported by the Heilongjiang Postdoctoral Fund [LBH-Z22120].

References

[1] Y. F. Nassar, M. J. Abdunnabi, M. N. Sbeta, A. A. Hafez, K. A. Amer, A. Y. Ahmed, B. Belgasim, Dynamic analysis and sizing optimization of a pumped hydroelectric storage-integrated hybrid PV/wind system: A case study, Energy Conversion and Management 229 (2021) 113744. URL: https://www.sciencedirect.com/science/article/pii/S0196890420312681. doi:10.1016/j.enconman.2020.113744.

[2] R. Perez, K. R. Rábago, M. Trahan, L. Rawlings, B. Norris, T. Hoff, M. Putnam, M. Perez, Achieving very high PV penetration – The need for an effective electricity remuneration framework and a central role for grid operators, Energy Policy 96 (2016) 27–35. URL: https://www.sciencedirect.com/science/article/pii/S0301421516302452. doi:10.1016/j.enpol.2016.05.016.

[3] C. Thai, J. Brouwer, Decarbonizing a solar PV and gas turbine microgrid with hydrogen and batteries, Energy Conversion and Management 292 (2023) 117391. URL: https://www.sciencedirect.com/science/article/pii/S0196890423007379. doi:10.1016/j.enconman.2023.117391.

[4] K. Klima, J. Apt, M. Bandi, P. Happy, C. Loutan, R. Young, Geographic smoothing of solar photovoltaic electric power production in the Western USA, Journal of Renewable and Sustainable Energy 10 (2018) 053504. URL: https://pubs.aip.org/aip/jrse/article/10/5/053504/1018177. doi:10.1063/1.5038028.

[5] S. Davarzani, I. Pisica, G. A. Taylor, K. J. Munisami, Residential demand response strategies and applications in active distribution network management, Renewable and Sustainable Energy Reviews 138 (2021) 110567. URL: ResidentialDemandResponseStrategiesandApplicationsinActiveDistributionNetworkManagement. doi:10.1016/j.rser.2020.110567.

[6] M. Perez, R. Perez, K. R. Rábago, M. Putnam, Overbuilding & curtailment: The cost-effective enablers of firm PV generation, Solar Energy 180 (2019) 412–422. URL: https://www.sciencedirect.com/science/article/pii/S0038092X18312714. doi:10.1016/j.solener.2018.12.074.

[7] Y. Li, S. Miao, B. Yin, J. Han, S. Zhang, J. Wang, X. Luo, Combined heat and power dispatch considering advanced adiabatic compressed air energy storage for wind power accommodation, Energy Conversion and Management 200 (2019) 112091. URL: https://www.sciencedirect.com/science/article/pii/S0196890419310970. doi:10.1016/j.enconman.2019.112091.

[8] M. J. Perez, R. Perez, T. E. Hoff, Ultra-high photovoltaic penetration: Where to deploy, Solar Energy 224 (2021) 1079–1098. URL: https://www.sciencedirect.com/science/article/pii/S0038092X21005259. doi:10.1016/j.solener.2021.06.041.

[9] M. Pierro, R. Perez, M. Perez, D. Moser, C. Cornaro, Italian protocol for massive solar integration: Imbalance mitigation strategies, Renewable Energy 153 (2020) 725–739. URL: https://www.sciencedirect.com/science/article/pii/S0960148120301671. doi:h10.1016/j.renene.2020.01.145.

[10] G. Yang, D. Yang, C. Lyu, W. Wang, N. Huang, J. Kleissl, M. J. Perez, R. Perez, D. Srinivasan, Implications of future price trends and interannual resource uncertainty on firm solar power delivery with photovoltaic overbuilding and battery storage, IEEE Transactions on Sustainable Energy In Press (2023) 1–13. URL: https://ieeexplore.ieee.org/document/10121691. doi:10.1109/TSTE.2023.3274109.

[11] R. Perez, M. Perez, J. Remund, K. Rabago, M. Putnam, M. Pierro, M. Prina, D. Moser, C. Cornaro, J. Schlemmer, J. Dise, T. E. Hoff, A. Swierc, P. Kellin, J. Boland, E. Tapaches, M. David, P. Lauret, R. van Eldik, W. van Sark, J. Lopez-Lorente, G. Makrides, G. E. Georghiou, Firm Power Generation–IEA PVPS Task 3.5 Report., Technical Report, International Energy Agency, 2023. URL: https://www.cleanpower.com/wp-content/uploads/PVPS_T16_A35_firmpvpower_report-preprint-2022.pdf.

[12] J. Remund, R. Perez, M. Perez, M. Pierro, D. Yang, Firm photovoltaic power generation: Overview and economic outlook, Solar RRL 7 (2023) 2300497. URL: https://onlinelibrary.wiley.com/doi/abs/10.1002/solr.202300497. doi:10.1002/solr.202300497.

[13] C. Cheng, L. Hughes, The role for offshore wind power in renewable hydrogen production in Australia, Journal of Cleaner Production 391 (2023) 136223. URL: https://www.sciencedirect.com/science/article/pii/S0959652623003815. doi:10.1016/j.jclepro.2023.136223.

[14] G. Yang, H. Zhang, W. Wang, B. Liu, C. Lyu, D. Yang, Capacity optimization and economic analysis of PV–hydrogen hybrid systems with physical solar power curve modeling, Energy Conversion and Management 288 (2023) 117128. URL: https://www.sciencedirect.com/science/article/pii/S0196890423004740. doi:10.1016/j.enconman.2023.117128.

[15] R. Li, X. Jin, P. Yang, X. Sun, G. Zhu, Y. Zheng, M. Zheng, L. Wang, M. Zhu, Y. Qi, Z. Huang, L. Zhao, D. Wang, W. Yang, Techno-economic analysis of a wind-photovoltaic-electrolysis-battery hybrid energy system for power and hydrogen generation, Energy Conversion and Management 281 (2023) 116854. URL: https://www.sciencedirect.com/science/article/pii/S0196890423002005. doi:10.1016/j.enconman.2023.116854.

[16] B. Zeng, L. Zhao, Solving two-stage robust optimization problems using a column-and-constraint generation method, Operations Research Letters 41 (2013) 457–461. URL: https://www.sciencedirect.com/science/article/pii/S0167637713000618. doi:10.1016/j.orl.2013.05.003.
[17] M. Tostado-Véliz, A. R. Jordehi, L. Fernández-Lobato, F. Jurado, Robust energy management in isolated microgrids with hydrogen storage and demand response, Applied Energy 345 (2023) 121319. URL: https://www.sciencedirect.com/science/article/pii/S0306261923006839. doi:10.1016/j.apenergy.2023.121319.
[18] W. Wang, D. Yang, N. Huang, C. Lyu, G. Zhang, X. Han, Irradiance-to-power conversion based on physical model chain: An application on the optimal configuration of multi-energy microgrid in cold climate, Renewable and Sustainable Energy Reviews 161 (2022) 112356. URL: https://www.sciencedirect.com/science/article/pii/S1364032122002660. doi:10.1016/j.rser.2022.112356.
[19] A. J. Gonzalez-Castellanos, D. Pozo, A. Bischi, Non-ideal linear operation model for Li-ion batteries, IEEE Transactions on Power Systems 35 (2020) 672–682. URL: https://ieeexplore.ieee.org/document/8770143. doi:10.1109/TPWRS.2019.2930450.
[20] Y. Jiang, W. Huang, G. Yang, Electrolysis plant size optimization and benefit analysis of a far offshore wind–hydrogen system based on information gap decision theory and chance constraints programming, International Journal of Hydrogen Energy 47 (2022) 5720–5732. URL: https://www.sciencedirect.com/science/article/pii/S0360319921046541. doi:10.1016/j.ijhydene.2021.11.211.
[21] M. Song, D. Yang, S. Lerch, G. M. Yagli, J. M. Bright, B. Liu, X. Liu, M. J. Mayer, X.-A. XIA, Y. Shen, Non-crossing quantile regression neural network as a calibration tool for ensemble weather forecasts, Advances in Atmospheric Sciences (2023). URL: http://www.iapjournals.ac.cn/aas/en/article/doi/10.1007/s00376-023-3184-5. doi:10.1007/s00376-023-3184-5.
[22] D. Yang, W. Wang, C. A. Gueymard, T. Hong, J. Kleissl, J. Huang, M. J. Perez, R. Perez, J. M. Bright, X. Xia, D. van der Meer, I. M. Peters, A review of solar forecasting, its dependence on atmospheric sciences and implications for grid integration: Towards carbon neutrality, Renewable and Sustainable Energy Reviews 161 (2022) 112348. URL: https://www.sciencedirect.com/science/article/pii/S1364032122002593. doi:10.1016/j.rser.2022.112348.
[23] D. Yang, W. Wang, X. Xia, A concise overview on solar resource assessment and forecasting, Advances in Atmospheric Sciences 39 (2022) 1239–1251. URL: https://link.springer.com/article/10.1007/s00376-021-1372-8. doi:10.1007/s00376-021-1372-8.
[24] M. J. Mayer, G. Gróf, Extensive comparison of physical models for photovoltaic power forecasting, Applied Energy 283 (2021) 116239. URL: https://www.sciencedirect.com/science/article/pii/S0306261920316330. doi:10.1016/j.apenergy.2020.116239.
[25] D. Yang, J. Kleissl, Solar Irradiance and Photovoltaic Power Forecasting, CRC Press, 2014.
[26] D. Hoadley, Efficient calculation of solar position using rectangular coordinates, Solar Energy 220 (2021) 80–87. URL: https://www.sciencedirect.com/science/article/pii/S0038092X21001213. doi:10.1016/j.solener.2021.02.019.
[27] I. Reda, A. Andreas, Solar position algorithm for solar radiation applications, Solar Energy 76 (2004) 577–589. URL: https://www.sciencedirect.com/science/article/pii/S0038092X0300450X. doi:10.1016/j.solener.2003.12.003.
[28] D. Yang, Estimating 1-min beam and diffuse irradiance from the global irradiance: A review and an extensive worldwide comparison of latest separation models at 126 stations, Renewable and Sustainable Energy Reviews 159 (2022) 112195. doi:10.1016/j.rser.2022.112195.
[29] D. Yang, C. A. Gueymard, Ensemble model output statistics for the separation of direct and diffuse components from 1-min global irradiance, Solar Energy 208 (2020) 591–603. URL: https://www.sciencedirect.com/science/article/pii/S0038092X2030582X. doi:10.1016/j.solener.2020.05.082.
[30] M. Sengupta, Y. Xie, A. Lopez, A. Habte, G. Maclaurin, J. Shelby, The National Solar Radiation Data Base (NSRDB), Renewable and Sustainable Energy Reviews 89 (2018) 51–60. URL: https://www.sciencedirect.com/science/article/pii/S136403211830087X. doi:10.1016/j.rser.2018.03.003.
[31] D. Yang, A correct validation of the National Solar Radiation Data Base (NSRDB), Renewable and Sustainable Energy Reviews 97 (2018) 152–155. URL: https://www.sciencedirect.com/science/article/pii/S1364032118306087. doi:10.1016/j.rser.2018.08.023.
[32] E. L. Maxwell, A quasi-physical model for converting hourly global horizontal to direct normal insolation, Technical Report SERI/TR-215-3087, Solar Energy Research Inst., Golden, CO (USA), 1987.
[33] C. A. Gueymard, REST2: High-performance solar radiation model for cloudless-sky irradiance, illuminance, and photosynthetically active radiation – Validation with a benchmark dataset, Solar Energy 82 (2008) 272–285. doi:10.1016/j.solener.2007.04.008.
[34] D. Yang, Solar radiation on inclined surfaces: Corrections and benchmarks, Solar Energy 136 (2016) 288–302. URL: https://www.sciencedirect.com/science/article/pii/S0038092X16302432. doi:10.1016/j.solener.2016.06.062.
[35] R. Perez, P. Ineichen, R. Seals, J. Michalsky, R. Stewart, Modeling daylight availability and irradiance components from direct and global irradiance, Solar Energy 44 (1990) 271–289. doi:10.1016/0038-092X(90)90055-H.
[36] D. L. King, J. A. Kratochvil, W. E. Boyson, Photovoltaic array performance model, Technical Report SAND2004-3535, Sandia National Laboratories, Albuquerque, NM (United States), 2004.
[37] W. De Soto, S. A. Klein, W. A. Beckman, Improvement and validation of a model for photovoltaic array performance, Solar Energy 80 (2006) 78–88. URL: https://www.sciencedirect.com/science/article/pii/S0038092X05002410. doi:10.1016/j.solener.2005.06.010.
[38] Y. Xie, M. Sengupta, A. Habte, A. Andreas, The "Fresnel Equations" for Diffuse radiation on Inclined photovoltaic Surfaces (FEDIS), Renewable and Sustainable Energy Reviews 161 (2022) 112362. URL: https://www.sciencedirect.com/science/article/pii/S1364032122002726. doi:https://doi.org/10.1016/j.rser.2022.112362.
[39] A. P. Dobos, PVWatts Version 5 Manual, Technical Report, National Renewable Energy Lab. (NREL), Golden, CO (United States), 2014. doi:10.2172/1158421.
[40] R. Sioshansi, P. Denholm, J. Arteaga, S. Awara, S. Bhattacharjee, A. Botterud, W. Cole, A. Cortés, A. De Queiroz, J. DeCarolis, et al., Energy-storage modeling: State-of-the-art and future research directions, IEEE Transactions on Power Systems 37 (2021) 860–875. URL: https://ieeexplore.ieee.org/document/9513574. doi:10.1109/TPWRS.2021.3104768.
[41] K. Antoniadou-Plytaria, D. Steen, O. Carlson, M. F. Ghazvini, et al., Market-based energy management model of a building microgrid considering battery degradation, IEEE transactions on smart grid 12 (2020) 1794–1804. URL: https://ieeexplore.ieee.org/document/9253666. doi:10.1109/TSG.2020.3037120.

[42] F. Wankmüller, P. R. Thimmapuram, K. G. Gallagher, A. Botterud, Impact of battery degradation on energy arbitrage revenue of grid-level energy storage, Journal of Energy Storage 10 (2017) 56–66. URL: https://www.sciencedirect.com/science/article/pii/S2352152X16303231. doi:10.1016/j.est.2016.12.004.
[43] Z. Ma, T. Tian, Q. Cui, J. Shu, J. Zhao, H. Wang, Rapid sizing of a hydrogen–battery storage for an offshore wind farm using convex programming, International Journal of Hydrogen Energy 48 (2023) 21946–21958. URL: https://www.sciencedirect.com/science/article/pii/S0360319923010509. doi:10.1016/j.ijhydene.2023.03.037.
[44] Z. Deng, Y. Jiang, Optimal sizing of wind–hydrogen system considering hydrogen demand and trading modes, International Journal of Hydrogen Energy 45 (2020) 11527–11537. URL: https://www.sciencedirect.com/science/article/pii/S0360319920306534. doi:10.1016/j.ijhydene.2020.02.089.
[45] M. Gökçek, Hydrogen generation from small-scale wind-powered electrolysis system in different power matching modes, International Journal of Hydrogen Energy 35 (2010) 10050–10059. URL: https://www.sciencedirect.com/science/article/pii/S0360319910015375. doi:10.1016/j.ijhydene.2010.07.149.
[46] C. Lamy, P. Millet, A critical review on the definitions used to calculate the energy efficiency coefficients of water electrolysis cells working under near ambient temperature conditions, Journal of Power Sources 447 (2020) 227350. URL: https://www.sciencedirect.com/science/article/pii/S0378775319313436. doi:10.1016/j.jpowsour.2019.227350.
[47] H. Ito, T. Maeda, A. Nakano, H. Takenaka, Properties of Nafion membranes under PEM water electrolysis conditions, International Journal of Hydrogen Energy 36 (2011) 10527–10540. URL: https://www.sciencedirect.com/science/article/pii/S0360319911013760. doi:10.1016/j.ijhydene.2011.05.127.
[48] F. Fouda-Onana, M. Chandesris, V. Médeau, S. Chelghoum, D. Thoby, N. Guillet, Investigation on the degradation of MEAs for PEM water electrolysers part I: Effects of testing conditions on MEA performances and membrane properties, International Journal of Hydrogen Energy 41 (2016) 16627–16636. URL: https://www.sciencedirect.com/science/article/pii/S0360319916321164. doi:10.1016/j.ijhydene.2016.07.125.
[49] M. Chandesris, V. Médeau, N. Guillet, S. Chelghoum, D. Thoby, F. Fouda-Onana, Membrane degradation in PEM water electrolyzer: Numerical modeling and experimental evidence of the influence of temperature and current density, International Journal of Hydrogen Energy 40 (2015) 1353–1366. URL: https://www.sciencedirect.com/science/article/pii/S0360319914032455. doi:10.1016/j.ijhydene.2014.11.111.
[50] Z. Abdin, C. J. Webb, E. M. Gray, Modelling and simulation of a proton exchange membrane (PEM) electrolyser cell, International Journal of Hydrogen Energy 40 (2015) 13243–13257. URL: https://www.sciencedirect.com/science/article/pii/S0360319915019321. doi:10.1016/j.ijhydene.2015.07.129.
[51] C. F. Jekel, G. Venter, pwlf: A Python Library for Fitting 1D Continuous Piecewise Linear Functions, 2019. URL: https://github.com/cjekel/piecewise_linear_fit_py.
[52] H. Liu, A. Almansoori, M. Fowler, A. Elkamel, Analysis of Ontario's hydrogen economy demands from hydrogen fuel cell vehicles, International Journal of Hydrogen Energy 37 (2012) 8905–8916. URL: https://www.sciencedirect.com/science/article/pii/S0360319912006301. doi:10.1016/j.ijhydene.2012.03.029.
[53] M. J. Perez, A model for optimizing the combination of solar electricity generation, supply curtailment, transmission and storage, Columbia University, 2014. URL: https://academiccommons.columbia.edu/doi/10.7916/D8445JP4. doi:10.7916/D8445JP4.
[54] X. Xu, B. Xu, J. Dong, X. Liu, Near-term analysis of a roll-out strategy to introduce fuel cell vehicles and hydrogen stations in Shenzhen China, Applied Energy 196 (2017) 229–237. doi:10.1016/j.apenergy.2016.11.048.
[55] Gurobi Optimization, LLC, Gurobi Optimizer Reference Manual, 2023. URL: https://www.gurobi.com.
[56] S. Wilcox, W. Marion, Users manual for TMY3 data sets, 2008. URL: https://www.osti.gov/biblio/928611. doi:10.2172/928611.
[57] National Solar Radiation Database, National Renewable Energy Laboratory, Learn about the TMY data type used in the NSRDB., 2023. URL: https://nsrdb.nrel.gov/data-sets/tmy., (2023, July 13).
[58] Ong, Sean, Clark, Nathan, Commercial and Residential Hourly Load Profiles for all TMY3 Locations in the United States, 2014. URL: https://data.openei.org/submissions/153. doi:10.25984/1788456.
[59] D. Yang, Validation of the 5-min irradiance from the National Solar Radiation Database (NSRDB), Journal of Renewable and Sustainable Energy 13 (2021) 016101. doi:10.1063/5.0030992.
[60] W. F. Holmgren, C. W. Hansen, M. A. Mikofski, pvlib python: A python package for modeling solar energy systems, Journal of Open Source Software 3 (2018) 884. doi:10.21105/joss.00884.
[61] D. Yang, SolarData: An R package for easy access of publicly available solar datasets, Solar Energy 171 (2018) A3–A12. URL: https://www.sciencedirect.com/science/article/pii/S0038092X18306583. doi:10.1016/j.solener.2018.06.107.
[62] H. Zhang, X. Zhang, D. Yang, Y. Shuai, B. G. Lougou, Q. Pan, F. Wang, Selection of iron-based oxygen carriers for two-step solar thermochemical splitting of carbon dioxide, Energy Conversion and Management 279 (2023) 116772. URL: https://www.sciencedirect.com/science/article/pii/S0196890423001188. doi:10.1016/j.enconman.2023.116772.
[63] G. Glenk, S. Reichelstein, Economics of converting renewable power to hydrogen, Nature Energy 4 (2019) 216–222. URL: https://www.nature.com/articles/s41560-019-0326-1#citeas. doi:10.1038/s41560-019-0326-1.
[64] Q. Chen, N. Lin, S. Bu, H. Wang, B. Zhang, Interpretable time-adaptive transient stability assessment based on dual-stage attention mechanism, IEEE Transactions on Power Systems (2022) 1–14. URL: https://ieeexplore.ieee.org/abstract/document/9802730/metrics#metrics. doi:10.1109/TPWRS.2022.3184981.
[65] R. Jiang, Y. Zheng, Series arc fault detection using regular signals and time-series reconstruction, IEEE Transactions on Industrial Electronics 70 (2023) 2026–2036. URL: https://ieeexplore.ieee.org/document/9756255. doi:10.1109/TIE.2022.3165260.
[66] Q. Chen, S. Bu, Impedance-based stability analysis of power system wideband oscillations: A bridge between s domain and frequency domain, IEEE Transactions on Power Systems (2023) 1–14. doi:10.1109/TPWRS.2023.3341432.
[67] Manualzz, Yingli YL250P-29b data sheet, 2015. https://manualzz.com/doc/11503449/yingli-yl250p-29b-data-sheet. Last accessed on July 11th, 2023.
[68] EnergySage, TMEIC solar inverters, 2012. https://www.energysage.com/solar-inverters/tmeic/2866/pvl-l0833gr/. Last ac-

cessed on July 11th, 2023.
[69] A. J. Gonzalez-Castellanos, D. Pozo, A. Bischi, Data for: A detailed Li-ion battery operation model, Mendeley Data, V1 (2018). URL: https://data.mendeley.com/datasets/36w7ts3r4t/1. doi:10.17632/36w7ts3r4t.1.
[70] A. Younis, A. Abdeljalil, A. Omer, Determination of panel generation factor using peaks over threshold method and short-term data for an off-grid photovoltaic system in Sudan: A case of Khartoum city, Solar Energy 249 (2023) 242–249. URL: https://www.sciencedirect.com/science/article/pii/S0038092X22008593. doi:10.1016/j.solener.2022.11.039.
[71] J. A. Onwuzuruike, M. A. Aminu, Experimental determination of panel generation factor for Apo Area of Federal Capital Territory in Nigeria, Journal of Scientific Research and Reports 24 (2019) 1–5. URL: https://journaljsrr.com/index.php/JSRR/article/view/1005. doi:10.9734/jsrr/2019/v24i330157.
[72] G. Yang, Y. Jiang, S. You, Planning and operation of a hydrogen supply chain network based on the off-grid wind–hydrogen coupling system, International Journal of Hydrogen Energy 45 (2020) 20721–20739. URL: https://www.sciencedirect.com/science/article/pii/S0360319920320619. doi:10.1016/j.ijhydene.2020.05.207.
[73] J. Turner, G. Sverdrup, M. K. Mann, P.-C. Maness, B. Kroposki, M. Ghirardi, R. J. Evans, D. Blake, Renewable hydrogen production, International Journal of Energy Research 32 (2008) 379–407. doi:10.1002/er.1372.
[74] F. Marini, B. Walczak, Particle swarm optimization (pso). A tutorial, Chemometrics and Intelligent Laboratory Systems 149 (2015) 153–165. URL: https://www.sciencedirect.com/science/article/pii/S0169743915002117. doi:10.1016/j.chemolab.2015.08.020.
[75] Y. Mu, W. Chen, X. Yu, H. Jia, K. Hou, C. Wang, X. Meng, A double-layer planning method for integrated community energy systems with varying energy conversion efficiencies, Applied Energy 279 (2020) 115700. URL: https://www.sciencedirect.com/science/article/pii/S0306261920311958. doi:10.1016/j.apenergy.2020.115700.
[76] A. Alkhalidi, K. Alqarra, M. A. Abdelkareem, A. G. Olabi, Renewable energy curtailment practices in Jordan and proposed solutions, International Journal of Thermofluids 16 (2022) 100196. URL: https://www.sciencedirect.com/science/article/pii/S266620272200060X. doi:10.1016/j.ijft.2022.100196.
[77] J. Park, K. Hwan Ryu, C.-H. Kim, W. Chul Cho, M. Kim, J. Hun Lee, H.-S. Cho, J. H. Lee, Green hydrogen to tackle the power curtailment: Meteorological data-based capacity factor and techno-economic analysis, Applied Energy 340 (2023) 121016. URL: https://www.sciencedirect.com/science/article/pii/S030626192300380X. doi:10.1016/j.apenergy.2023.121016.
[78] M. Younas, S. Shafique, A. Hafeez, F. Javed, F. Rehman, An overview of hydrogen production: Current status, potential, and challenges, Fuel 316 (2022) 123317. URL: https://www.sciencedirect.com/science/article/pii/S0016236122001867. doi:10.1016/j.fuel.2022.123317.
[79] State Grid Corporation of China, International comparative analysis for the electricity prices of China, 2021. URL: http://www.sasac.gov.cn/n16582853/n16582883/c17715327/content.html., (2023, February 13).
[80] State Administration of Foreign Exchange, Table of the exchange rate of various currencies against to the US Dollar (2019, December 31)., 2019. URL: http://m.safe.gov.cn/safe/2019/1231/15022.html., (2023, July 13).
[81] M. Zhang, Q. Zhang, Grid parity analysis of distributed photovoltaic power generation in China, Energy 206 (2020) 118165. URL: https://www.sciencedirect.com/science/article/pii/S036054422031272X. doi:10.1016/j.energy.2020.118165.
[82] Clifford Chance, E-fuels and green ammonia–the solution for decarbonising shipping and heavy transport?, 2022. URL: https://www.cliffordchance.com/briefings/2022/10/e-fuels-and-green-ammonia---the-solution-for-decarbonising-shipp.html, (2023, July 13).